

# Decentralized GNSS at Global Scale via Graph-Aware Diffusion Adaptation

Xue Xian Zheng, Xing Liu\*, and Tareq Y. Al-Naffouri

**Abstract**—Network-based Global Navigation Satellite Systems (GNSS) underpin critical infrastructure and autonomous systems, yet typically rely on centralized processing hubs that limit scalability, resilience, and latency. Here we report a global-scale, decentralized GNSS architecture spanning hundreds of ground stations. By modeling the receiver network as a time-varying graph, we employ a deep linear neural network approach to learn topology-aware mixing schedules that optimize information exchange. This enables a gradient tracking diffusion strategy wherein stations execute local inference and exchange succinct messages to achieve two concurrent objectives: centimeter-level self-localization and network-wide consensus on satellite correction products. The consensus products are broadcast to user receivers as corrections, supporting precise point positioning (PPP) and precise point positioning–real-time kinematic (PPP-RTK). Numerical results demonstrate that our method matches the accuracy of centralized baselines while significantly outperforming existing decentralized methods in convergence speed and communication overhead. By reframing decentralized GNSS as a networked signal processing problem, our results pave the way for integrating decentralized optimization, consensus-based inference, and graph-aware learning as effective tools in operational satellite navigation.

**Index Terms**—GNSS, decentralized optimization, gradient tracking, diffusion strategies, time-varying graphs, PPP/PPP-RTK.



## 1 INTRODUCTION

High-precision Global Navigation Satellite Systems (GNSS) provide the foundational layer for applications ranging from autonomous transport to crustal deformation monitoring. To achieve centimeter-level precision—such as in precise point positioning (PPP) [1], [2] and precise point positioning–real-time kinematic (PPP-RTK) [3] modes—user receivers rely on network-derived products, including precise satellite clocks, orbits, and atmospheric corrections. Historically, these products are estimated in a centralized manner: observations from global networks of continuously operating reference stations (CORS) are streamed to a single analysis center for joint processing [4]–[6]. While effective at current scales, this centralized paradigm is approaching a critical threshold, strained by an exponential increase in data volume and network density.

The rapid expansion of multi-constellation tracking and the imminent integration of Low Earth Orbit (LEO) augmented GNSS are creating a “big data” regime characterized by high observation densities and short update intervals [7], [8]. The proposed LEO constellations alone comprise on the order of 60k satellites in the next five years. Although only a

subset of these LEO constellations is explicitly designed for navigation, an increasing number of non-dedicated systems are being actively explored by the GNSS community as signals of opportunity for positioning, thereby potentially enabling an unprecedented number of spaceborne transmitters to be leveraged for navigation [9]. In this context, centralized processing creates severe vulnerabilities, including prohibitive computational complexity, bandwidth saturation from raw data backhaul, and latency in product dissemination. Moreover, reliance on a monolithic analysis hub introduces a resilience bottleneck, where node failures or link congestion can compromise the entire service. To support the next generation of instantaneous, ubiquitous positioning, the computational burden must shift from the center to the edge.

Decentralized architectures [10], [11] offer a compelling response to these systemic vulnerabilities, as evidenced by the recent success of distributed systems in blockchain networks [12], large-scale training on neural models [13], and robotic swarm intelligence [14]. In these paradigms, computation and storage are moved away from a single monolithic server and distributed across many loosely coupled nodes, which exchange only compact, high-level information (e.g., gradients, model updates, or consensus variables) rather than raw data streams [11]. This shift enables systems that scale with the number of participants, improve robustness through redundancy, and adapt locally to heterogeneous conditions, while maintaining low end-to-end latency [13].

*The authors are with the Electrical and Computer Engineering Program, Computer, Electrical and Mathematical Sciences and Engineering Division, King Abdullah University of Science and Technology (KAUST), Thuwal 23955-6900, Saudi Arabia.*

*\*Corresponding author. e-mail: xing.liu@kaust.edu.sa.*



Fig. 1. Decentralized GNSS receiver network used in this work: a sparse, global graph with 100 nodes placed at selected IGS station locations. Red points denote nodes; black lines denote communication links. The depicted communication pattern yields a graph characterized by 182 edges, a diameter of 12, and a radius of 10. Note that this represents a single instance; patterns can change under different protocols, and the associated mixing weights that govern information exchange between nodes also vary; together, these constitute a time-varying communication graph.

Translating these ideas to GNSS networks is particularly promising. Decentralized processing could not only alleviate central bottlenecks but also enable new classes of real-time services. Edge nodes—such as regional hubs or even high-end user receivers—can perform local preprocessing, quality control, and partial estimation of satellite and atmospheric parameters, exchanging only succinct correction updates or state summaries with neighboring nodes and a lightweight coordination layer. However, the realization of truly decentralized high-precision GNSS is still at an early stage. Yet the idea of distributing the processing workload across the network traces back more than a decade. Boomkamp’s DANCER system for large geodetic networks [15] and the consensus-based distributed filtering framework of Khodabandeh and Teunissen [16] already anticipated the some challenges of scaling to dense, global GNSS infrastructures. Building on this vision, Khodabandeh and Teunissen [17] recast the classical network adjustment problem on a communication graph and solved it with alternating direction method of multipliers (ADMM), showing that decentralized satellite code-bias estimates can approach the accuracy of a centralized baseline in static, well-connected networks. More recently, Hou and Zhang [18] focused on the generation of PPP-RTK network-derived products, proposing a subnetwork-based PPP-RTK strategy that matches centralized accuracy at roughly half the computational cost. Together, these contributions mark the first steps away from monolithic processing towards archi-

tectures that are compatible with the emerging, data-rich GNSS ecosystem, but they remain only partially decentralized and largely overlook the rich structure of underlying communication graphs.

Here we propose a global-scale, decentralized GNSS architecture that treats the receiver network as a time-varying, sparsely connected graph and generates network-derived products, building on recent advances in networked signal and information processing (SIP) [19], [20]. Receivers are modeled as nodes and intermittent communication links as edges (**Figure 1**). For a given set of communication patterns, we learn topology-aware, doubly stochastic mixing weights and time-varying combination schedules offline. We interpret the product of the time-varying mixing matrices as a deep linear neural network and train it to approximate the consensus operator (**Figure 2, Left Panel; Figure 3**). This yields a fully decentralized online diffusion strategy that applies these weights to achieve fast convergence. By modeling both local receiver states and global satellite parameters as latent graph signals, the centralized solution is recovered using only local computation and succinct message exchanges (**Figure 2, Right Panel**). Instantiating the architecture on a simulated global GNSS network built from the geodetic coordinates of hundreds of IGS stations and RINEX navigation files, we show that the decentralized estimates match a centralized baseline with centimeter-level positioning error, while converging faster than existing decentralized counterparts and reducing communication

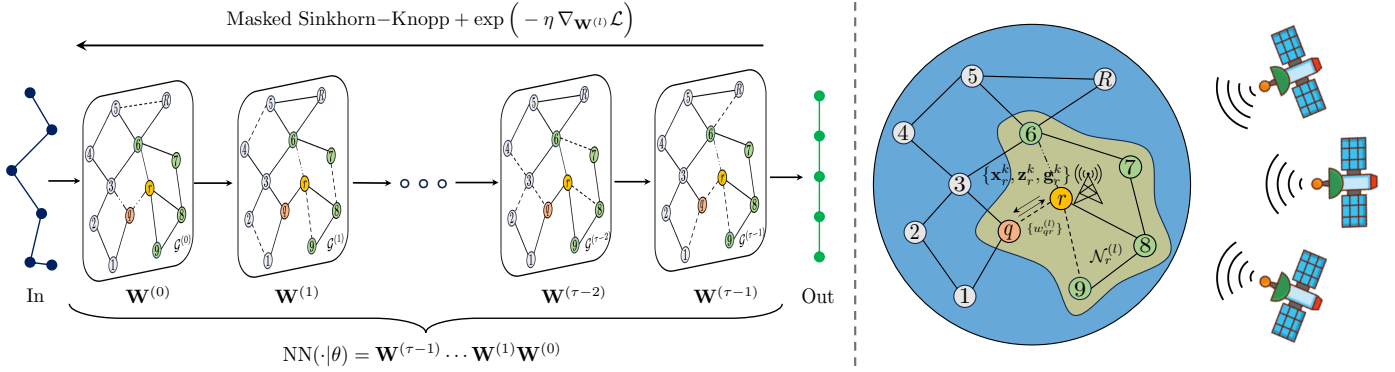


Fig. 2. (Left.) Learning graph-aware mixing sequence  $\theta = \{\mathbf{W}^{(l)}\}_{l=0}^{\tau-1}$  on time-varying graph  $\mathcal{G}^{(l)} = (\mathcal{V}, \mathcal{E}^{(l)}, \mathbf{W}^{(l)})$ . We regard the product  $\text{NN}(\cdot|\theta) = \mathbf{W}^{(\tau-1)} \dots \mathbf{W}^{(0)}$  as a deep linear neural network and optimize  $\theta$  via exponentiated-gradient updates, masking, and row/column scaling. This enforces each  $\mathbf{W}^{(l)}$  to be doubly stochastic while driving the product toward the consensus operator  $\frac{1}{R} \mathbf{1}\mathbf{1}^\top$  with small error  $\epsilon_\tau$ . (Right.) ATC GT-Diffusion scheme with  $\theta$  for GNSS network. Each receiver  $r \in \mathcal{V}$  updates its state  $(\mathbf{x}_r^k, \mathbf{z}_r^k)$  and GT variable  $\mathbf{g}_r^k$  at iteration  $k$ . Updates use (i) local observations from the visible satellites and (ii) messages from neighbors  $\mathcal{N}_r^{(l)}$ , combined via mixing weight  $w_{rq}^k$  for  $q \in \mathcal{N}_r^{(l)}$  over a time-varying graph  $\mathcal{G}^{(l)}$ . Here  $l = k \bmod \tau$ , i.e.,  $\mathbf{W}^{(l)}$  is sampled  $\tau$ -periodically from  $\theta$  across  $k$ , which promotes convergence.

overhead (Figure 4, Figure 5). We also detail the training procedure for the deep linear neural network and provide rigorous convergence guarantees for the resulting diffusion strategies, proving linear convergence rates (Methods and Supplementary Notes).

## 2 RESULTS

### 2.1 The Overall Design

The proposed global-scale, decentralized GNSS architecture operates as a two-stage system, as illustrated in Figure 2. The first stage is an offline graph-aware learning phase that derives a sequence of doubly stochastic mixing matrices tailored to a set of known communication patterns. The second stage is an online optimization phase that executes an adapt-then-combine (ATC) diffusion strategy augmented with gradient tracking (GT). In this phase, nodes exchange global satellite parameters and gradient trackers to reach consensus on global states while simultaneously optimizing local parameters. These stages are tightly coupled in a framework we term **Graph-Aware ATC GT-Diffusion**: the offline phase overcomes the limitations of single-snapshot topology optimization by maximizing information mixing over time, thereby significantly accelerating the online phase's convergence to the centralized baseline.

### 2.2 Agreement on Satellite Parameters

We partition the GNSS parameter space at receiver  $r$  into two distinct components: a local state  $\mathbf{x}_r$  (capturing unique parameters such as incremental position, receiver clock offsets, atmospheric delays, and carrier-phase ambiguities) and a shared global state  $\mathbf{z}$  (encompassing satellite clocks and

hardware biases). This decomposition yields a streamlined linearized observation model:

$$\mathbf{y}_r = \mathbf{A}_r \mathbf{x}_r + \mathbf{B}_r \mathbf{z} + \mathbf{n}_r, \quad (1)$$

where  $\mathbf{y}_r$  denotes the observation vector,  $\mathbf{A}_r$  and  $\mathbf{B}_r$  are the design matrices, and  $\mathbf{n}_r$  represents measurement noise.

Because  $\mathbf{z}$  represents the physical properties of the satellite common to all observers, it mathematically couples the estimation tasks throughout the network. Standard centralized approaches resolve this coupling by aggregating high-dimensional raw data at a single fusion center—a process that scales poorly. By contrast, we demonstrate that our framework enables nodes to reach strict consensus on the global variable  $\mathbf{z}$  solely through compact peer-to-peer exchanges. This allows the network to recover the precise centralized solution while minimizing local objectives and maintaining communication efficiency (see Methods for full formulation details).

### 2.3 Communication graphs, Patterns and Graph-Aware Fast Mixing Weights

As seen in Figure 1, we model the GNSS infrastructure not as a static hierarchy, but as a time-varying communication graph  $\mathcal{G}^{(l)} = (\mathcal{V}, \mathcal{E}^{(l)}, \mathbf{W}^{(l)})$ . Here, the  $R$  receivers form the node set  $\mathcal{V} = \{1, \dots, R\}$ , while the edge set  $\mathcal{E}^{(l)} \subseteq \mathcal{V} \times \mathcal{V}$  represents time-varying communication links governed by bandwidth constraints and exchange protocols. To orchestrate information flow, each snapshot is assigned a mixing matrix  $\mathbf{W}^{(l)} = [w_{rq}^{(l)}] \in \mathbb{R}^{R \times R}$ , compatible with the topology, where  $w_{rq}^{(l)} > 0$  only if receivers  $r$  and  $q$  can communicate. We enforce that  $\mathbf{W}$  is doubly stochastic ( $\mathbf{W}^{(l)} \mathbf{1} = \mathbf{1}, \mathbf{1}^\top \mathbf{W}^{(l)} = \mathbf{1}^\top$ ), ensuring that the local averaging steps preserve the global mean of the estimated parameters.

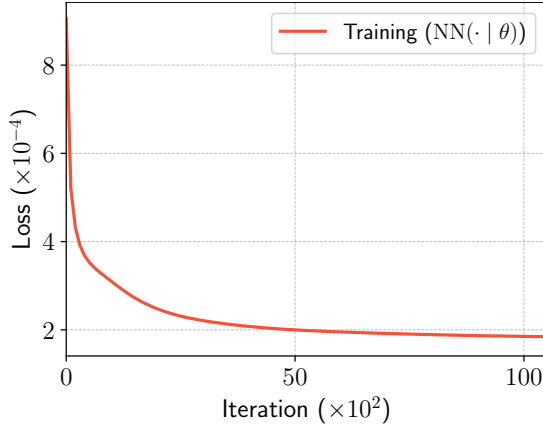


Fig. 3. Training  $\text{NN}(\cdot|\theta)$  via Algorithm 1 for the first  $10^4$  iteration. We employ the “Lazy” parameterization  $\frac{\mathbf{W}^{(l)+\mathbf{I}}}{2}$  at each layer to stabilize the subsequent online diffusion stage; this counteracts the effect of substantial data heterogeneity arising from potentially distinct satellite subsets observed by each receiver.

A fundamental challenge in such global-scale networks is that the graph may be sparsely connected—or even momentarily disconnected—at any single instant. To overcome this, our framework leverages the **block contraction property** over a time window  $\tau \in \mathbb{N}_{\geq 1}$ . Rather than requiring instantaneous connectivity, we interpret the sequence of communication graphs as layers in a deep linear neural network  $\text{NN}(\cdot|\theta)$  (see Figure 2) and optimize the mixing weights  $\theta = \{\mathbf{W}^{(l)}\}_{l=0}^{\tau-1}$  such that their cumulative product approximates the ideal global averaging operator:

$$\|\mathbf{W}^{(\tau-1)} \dots \mathbf{W}^{(1)} \mathbf{W}^{(0)} - \frac{1}{R} \mathbf{1}\mathbf{1}^\top\| = \epsilon_\tau. \quad (2)$$

Here  $\epsilon_\tau < 1$  is the spectral contraction factor over the window, with smaller values implying stronger contraction and faster consensus for fixed  $\tau$ . In homogeneous data settings,  $\epsilon_\tau$  can be driven arbitrarily close to zero when  $\tau$  is chosen between the graph diameter and roughly twice the graph radius, as suggested by previous work [21], [22]. Several graph families even admit exact  $\tau$ -step averaging with  $\epsilon_\tau = 0$ , yielding *finite-time consensus* with closed-form communication patterns and weights [23]–[25], which significantly reduces communication overhead while accelerating convergence for decentralized methods. While these successes highlight a compelling opportunity for the co-optimization of physical GNSS receiver placement and communication patterns, existing infrastructure is calling for solutions that remain effective under prescribed topologies.

For the global IGS network with the exemplified communication pattern shown in Figure 1, we select a window length of  $\tau = 15$  and reparameterize each layer in  $\text{NN}(\cdot|\theta)$  as  $\frac{\mathbf{W}^{(l)+\mathbf{I}}}{2}$  (see **Methods** for details on this reparameterization trick). Under this configuration, training converges to a final loss of  $1.77 \times 10^{-4}$  (Figure 3), corresponding to  $\epsilon_\tau = 0.68$ .

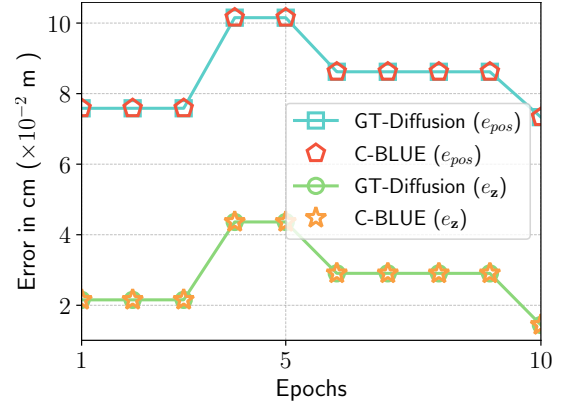


Fig. 4. Accuracy evaluation between Graph-Aware ATC GT-Diffusion and centralized solution (C-BLUE), exemplified by 10 epochs, containing local receiver’s positioning error  $e_{\text{pos}}$  and global satellite-bias error  $e_z$ . We report  $e_z$  in light-travel distance (equivalent range) units for consistency. Here, the maximum difference of  $e_{\text{pos}}$  and  $e_z$  between ATC GT-Diffusion and C-BLUE are  $6.88 \times 10^{-9}\text{m}$  and  $5 \times 10^{-9}\text{m}$ , respectively, occurring at epoch 5.

## 2.4 Graph-Aware ATC GT-Diffusion Recovers the Centralized Solution

We validated the proposed GNSS network using simulated measurements from 105 satellites across the GPS, GLONASS, Galileo, and BeiDou constellations, derived from RINEX navigation files. Our method, Graph-Aware ATC GT-Diffusion, integrates a standard online GT algorithm (see **Methods** for details on the algorithm) with a learned, graph-aware mixing weights  $\theta$ .

We defined the local state vector  $\mathbf{x}_r$  to encompass the receiver’s incremental position, clock bias, and float ambiguity terms, leaving integer ambiguity resolution for a subsequent processing stage. The global consensus variable  $\mathbf{z}$  captures the satellite-specific biases, with the first satellite fixed as a reference (bias set to zero) to ensure identifiability of the problem. Performance was benchmarked against the centralized Best Linear Unbiased Estimator (C-BLUE) [26] utilizing two standard metrics relative to ground truth: the average relative positioning error  $e_{\text{pos}}$  and the mean absolute satellite bias error  $e_z$ . We initialize all satellite-bias estimates, except for the reference satellite, to zero, corresponding to a stringent cold-start scenario in which the network has no prior information. In practical deployments, GNSS estimation is typically run recursively and uses the previous epoch’s solution as a prior, placing the initialization close to the optimum and leading to substantially faster convergence than in the pessimistic setting studied here.

As shown in Figure 4, our method achieves centimeter-level parity with the centralized baseline in exemplified 10 epochs. The maximum Euclidean discrepancies are negligible:  $6.88 \times 10^{-9}\text{m}$  for positioning error and  $5 \times 10^{-9}\text{m}$  (light-travel distance) for satellite bias. This equivalence is

TABLE 1  
Mahalanobis distance  $d_M(\mathbf{z})$  corresponding to Fig. 4

Epoch	1	2	3	4	5	6	7	8	9	10
C-BLUE [26]	11.1226...	11.1226...	11.1226...	9.3236...	9.3236...	8.6940...	8.6940...	8.6940...	8.6940...	9.0973...
Our Method	-	-	-	-	-	-	-	-	-	-
Difference	$7.82 \times 10^{-9}$	$-1.92 \times 10^{-8}$	$1.67 \times 10^{-8}$	$2.58 \times 10^{-8}$	$3.42 \times 10^{-8}$	$-2.02 \times 10^{-8}$	$2.08 \times 10^{-8}$	$1.87 \times 10^{-8}$	$1.12 \times 10^{-8}$	$-4.91 \times 10^{-10}$

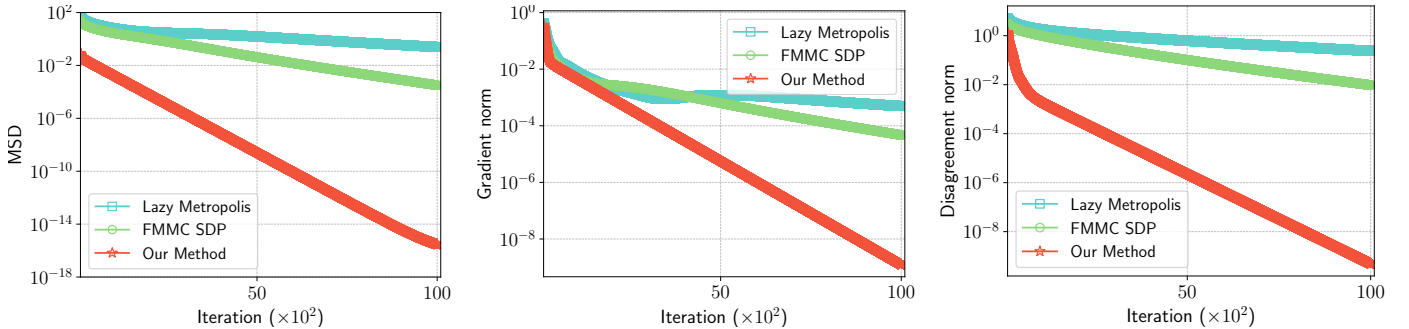


Fig. 5. Time-varying graphs improve convergence without additional communication overhead. All curves are plotted starting at iteration  $k = 10^2$ . For such a large and sparse graph as depicted in Fig. 1, here the Lazy Metropolis and FMMC yield mixing weights with the second-largest eigenvalue  $\lambda_2 = 0.989, 0.979$ , respectively.

further corroborated by the Mahalanobis distance  $d_M(\mathbf{z})$  against ground truth (Table 1), which utilizes the centralized precision matrix  $\Sigma^{-1}$  to assess statistical consistency. As detailed in Table 1, the divergence between the distributed and centralized solutions is restricted to the magnitude range  $[4.91 \times 10^{-10}, 3.42 \times 10^{-8}]$ , indicating extremely tight statistical agreement. Taken together, these results show that Graph-Aware ATC GT-Diffusion effectively recovers the centralized solution—both in Euclidean and statistical terms—while relying solely on sparse, peer-to-peer communication.

## 2.5 Graph-Aware ATC GT-Diffusion Accelerates Linear Convergence with Reduced Communication

To characterize both optimization and consensus behaviour, we monitor three per-iteration metrics: (i) the mean-square deviation (MSD) from the centralized solution, (ii) the average gradient norm, serving as a proxy for first-order optimality; and (iii) the network disagreement norm, quantifying the deviation of local nodes from the global average (see **Supplementary Notes** for formal definitions). We compare Graph-Aware ATC GT-Diffusion against two diffusion-based counterparts, both implemented within the same GT framework and using the communication pattern shown in Figure 1. The first uses heuristic Lazy Metropolis weights [27], while the second relies on weights obtained from the Fastest Mixing Markov Chain (FMMC) design [28], where a single mixing matrix is optimized via semidefinite programming (SDP) simultaneously promoting non-negative eigenvalues. In our notation, the FMMC baseline corresponds to optimizing the product in (2) with a win-

TABLE 2  
Summary on the SOTA decentralized GNSS framework

Framework	Ours	Khod.&Teunissen [17]
Constraint set	N ✓	Y ✗
Cluster averaging	N ✓	Y ✗
Time-var. graph	Y ✓	N ✗
Convergence	Y ✓	Y ✓

dow length of  $\tau = 1$ , i.e., a single-snapshot design. For illustration, we report results for a representative epoch (epoch 7). As shown in Figure 5, Graph-Aware ATC GT-Diffusion exhibits a markedly steeper linear decay in all three metrics than either of the baselines, with theoretical justification provided in the **Supplementary Notes**. In other words, to reach the same error tolerance relative to the centralized solution, our method requires far fewer iterations. Because each iteration uses the same sparse communication pattern, this translates directly into a substantial reduction in communication overhead. The gain stems from the reduced contraction factor  $\epsilon_\tau$  achieved by the learned,  $\tau$ -periodic schedule of mixing weights, which enables faster information diffusion over the same underlying network.

## 2.6 Structural Advantages over Standard Decentralized GNSS Network

We provide a side-by-side comparison between our framework and the decentralized ADMM-based GNSS architecture of Khod.&Teunissen [17], summarized in Table 2. The approach in Khod.&Teunissen [17] typically relies on a

hand-crafted, overlapping set of constraint nodes to enable intra-cluster hard averaging and promote convergence in practice. For large, time-varying networks such as in Figure 1, however, constructing and maintaining these overlapping clusters can be fragile, and may require manual retuning as the topology or station set evolves. By contrast, Graph-Aware ATC GT-Diffusion uses a unified GT framework with learned mixing weights and does not require any explicit cluster construction or overlap design, making it inherently more robust to graph variations.

More broadly, our method belongs to the class of gradient-driven algorithms: each node updates using local gradients together with neighbour state exchanges, rather than the constraint-heavy primal–dual machinery of ADMM. This lightweight structure is more tolerant to packet losses, link failures, and bandwidth fluctuations, since missing messages perturb only incremental gradient steps instead of disrupting coupled subproblems. With a single round of peer-to-peer communication per iteration and rigorous convergence guarantees on sparse, time-varying graphs, the proposed framework is particularly advantageous for next-generation regimes—such as GNSS constellations augmented by massive LEO fleets. In these data-dense, bandwidth-constrained environments, the integration of learned, graph-aware mixing policies with a controllable contraction factor  $\epsilon_\tau$  provides a principled and scalable pathway for decentralized global processing.

### 3 DISCUSSION AND FUTURE WORK

We have presented a fully decentralized architecture that resolves the GNSS network estimation problem using a Graph-Aware ATC GT-Diffusion scheme. To our knowledge, this represents the first step toward realizing decentralized GNSS networks capable of operating over time-varying graphs. Our method attains the centralized solution through strictly local computations and neighbor exchanges, with convergence established at a linear rate. Furthermore, this work investigates the impact of graph structures on convergence speed, communication overhead, and system robustness—factors that are pivotal to addressing the “big data” challenges inherent in modern satellite constellations.

The present work focuses on batched network estimation within each epoch. An important direction for future research is to extend the framework to fully streaming operation, in which tracking gradient and consensus are performed epoch-by-epoch, enabling continual decentralized learning as new measurements arrive. Such extensions would exploit the temporal structure of GNSS data and further reduce latency. Moreover, the framework is inherently compatible with fast-switching topologies, positioning it as

a promising building block for future spaceborne, onboard GNSS networks.

## 4 METHODS

We detail here the GNSS observation model, the decentralized problem formulation, the training procedure for  $\text{NN}(\cdot|\theta)$  and the associated GT diffusion framework. Unless otherwise specified, we use the following conventions. Non-bold lowercase and uppercase letters denote scalars; bold lowercase letters denote column vectors; bold uppercase letters denote matrices.  $\mathbf{1}$  is the all-ones vector of appropriate size, and  $\mathbf{I}_d$  is the  $d \times d$  identity matrix.  $\text{diag}(\cdot)$  returns a diagonal matrix,  $\text{blkdiag}(\cdot)$  returns a block-diagonal matrix, and  $\text{col}(\cdot)$  denotes vertical (column-wise) stacking of its arguments, respectively. We use  $\mathbb{E}(\cdot)$  and  $\mathbb{C}(\cdot, \cdot)$  to denote the expectation and covariance operators. The Hadamard and Kronecker products are denoted by  $\odot$  and  $\otimes$ , respectively. We write  $\|\cdot\|$  for the Euclidean norm of a vector; for matrices, it denotes the spectral norm,  $\|\cdot\|_F$  is the Frobenius norm, and  $\|\cdot\|_*$  is nuclear norm.

### 4.1 Observation Model and Decentralized Formulation

The linearized carrier-phase and pseudo-range (code) GNSS observation equations are given by

$$\begin{aligned} \Delta\phi_{r,j}^s(i) &= \mathbf{g}_r^s(i)^T \Delta\mathbf{p}_r(i) + dt_r(i) + \lambda_j \delta_{r,j}(i) - dt^s(i) - \lambda_j \delta_j^s(i) \\ &\quad + v_r^s(i) \tau_r(i) - \mu_j l_r^s(i) + \lambda_j a_{r,j}^s + \epsilon_{\phi,r,j}^s(i), \\ \Delta\rho_{r,j}^s(i) &= \mathbf{g}_r^s(i)^T \Delta\mathbf{p}_r(i) + dt_r(i) + d_{r,j}(i) - dt^s(i) - d_j^s(i) \\ &\quad + v_r^s(i) \tau_r(i) + \mu_j l_r^s(i) + \epsilon_{\rho,r,j}^s(i). \end{aligned} \quad (3)$$

Wherein:

- $\Delta\phi_{r,j}^s(i)$  and  $\Delta\rho_{r,j}^s(i)$  represent the observed-minus-computed undifferenced carrier-phase and pseudo-range observations, respectively.
- The indices  $r, s, j$ , and  $i$  denote the receiver, satellite, frequency, and epoch indices, respectively.
- $\mathbf{g}_r^s(i)$  is the line-of-sight unit vector.
- $\Delta\mathbf{p}_r(i)$  denotes the incremental receiver position.
- $dt_r(i)$  and  $dt^s(i)$  are the receiver and satellite clock offsets, respectively.
- $\delta_{r,j}(i)$  and  $\delta_j^s(i)$  denote the receiver and satellite carrier-phase hardware biases, respectively.
- $d_{r,j}(i)$  and  $d_j^s(i)$  denote the receiver and satellite pseudo-range hardware biases, respectively.
- $\tau_r(i)$  is the zenith tropospheric delay, with  $v_r^s(i)$  being the corresponding tropospheric mapping function coefficient.
- $l_r^s(i)$  refers to the ionospheric delay on the first frequency. The coefficient  $\mu_j = \lambda_j^2/\lambda_1^2$  is defined using  $\lambda_j$ , the wavelength corresponding to frequency  $j$ .
- $a_{r,j}^s$  denotes the carrier-phase ambiguity.

- Finally,  $\varepsilon_{\phi,r,j}^s(i)$  and  $\varepsilon_{\rho,r,j}^s(i)$  denote the observation noise terms.

Consider a receiver network with nodes  $r = 1, \dots, R$ . Each node  $r$  collects an observation vector  $\mathbf{y}_r$  consisting of observed-minus-computed, undifferenced carrier-phase and pseudo-range measurements. The measurement noise  $\mathbf{n}_r$  is assumed to have zero mean,  $\mathbb{E}(\mathbf{n}_r) = \mathbf{0}$ , and covariance  $\mathbf{Q}_r$ , with  $\mathbb{C}(\mathbf{n}_r, \mathbf{n}_{r'}) = \delta_{rr'} \mathbf{Q}_r$ , where  $\delta_{rr'}$  denotes the Kronecker delta.

The estimation variables at receiver  $r$  are organized into a local state  $\mathbf{x}_r$  and a set of satellite-specific parameters collected in a global state  $\mathbf{z}$ . Different system models may be adopted. For instance, when some receivers serve as reference stations, their positions can be treated as known. Additional satellite-related parameters, such as orbit corrections, may also be included in the global state vector. Regardless of the specific modeling choices, the parameters can always be organized into a local state  $\mathbf{x}_r$  and a global state  $\mathbf{z}$ . Under this representation, the linearized observation model admits the compact form (1) used in the **Results** section. It is important to note that  $\mathbf{x}_r$  and  $\mathbf{z}$  represent identifiable parameterizations derived from the original undifferenced observation model in (3). These parameterizations preserve the physical interpretability of the underlying parameters while ensuring full rank of the network design matrix. A detailed discussion is omitted for brevity.

A scalable decentralized formulation can be written as follows:

$$\underset{\{\mathbf{x}_r\}_{r=1}^R, \mathbf{z}}{\text{minimize}} \quad f(\{\mathbf{x}_r\}_{r=1}^R, \mathbf{z}) = \sum_{r=1}^R f_r(\mathbf{x}_r, \mathbf{z}), \quad (4)$$

$$\text{where } f_r(\mathbf{x}_r, \mathbf{z}) = \frac{1}{2} \|\mathbf{A}_r \mathbf{x}_r + \mathbf{B}_r \mathbf{z} - \mathbf{y}_r\|_{\mathbf{Q}_r^{-1}}^2.$$

Under this formulation, each node minimizes its local objective  $f_r(\mathbf{x}_r, \mathbf{z})$  while exchanging only compact information with neighboring nodes.

## 4.2 Learning Graph-Aware Mixing Sequence

$\theta$  can be learned by solving the surrogate problem

$$\begin{aligned} & \underset{\theta = \{\mathbf{W}^{(l)}\}_{l=0}^{\tau-1}}{\text{minimize}} \quad \mathcal{L} = \|\text{NN}(\cdot|\theta) - \frac{1}{R} \mathbf{1} \mathbf{1}^\top\|_F^2 \\ & \text{subject to} \quad \text{NN}(\cdot|\theta) = \mathbf{W}^{(\tau-1)} \dots \mathbf{W}^{(1)} \mathbf{W}^{(0)}, \\ & \quad \mathbf{W}^{(l)} \mathbf{1} = \mathbf{1}, \mathbf{1}^\top \mathbf{W}^{(l)} = \mathbf{1}^\top, \\ & \quad [\mathbf{W}^{(l)}]_{rq} = 0 \text{ if } (r, q) \notin \mathcal{E}^{(l)}, \\ & \quad \mathbf{W}^{(l)} \geq 0, \quad l = 0, \dots, \tau - 1. \end{aligned} \quad (5)$$

As we can see, gradients  $\{\nabla_{\mathbf{W}^{(l)}} \mathcal{L}\}_{l=0}^{\tau-1}$  could be computed by backpropagation through the product. The main difficulty is enforcing, at every layer  $l$ , (i) nonnegativity, (ii) the graph-induced sparsity pattern, and (iii) double stochasticity. To address this, we apply an exponentiated-gradient

---

Algorithm 1. Learning Mixing Sequence via Masked Sinkhorn–Knopp

**Input:** Window length  $\tau$ ; mask matrices  $\{\mathbf{M}^{(l)}\}_{l=0}^{\tau-1} \in \{0, 1\}^{R \times R}$ ; stepsize  $\eta > 0$ ; maximum training iterations  $\mathcal{K}$ ; initialization  $\{\mathbf{W}^{(l)} \geq 0\}$  with support  $\mathbf{M}^{(l)}$

**Output:** Mixing matrices  $\theta = \{\mathbf{W}^{(l)}\}_{l=0}^{\tau-1}$

- 1: **for**  $\kappa = 0, 1, \dots, \mathcal{K} - 1$  **do**
  - 2:    $\text{NN}(\cdot|\theta) \leftarrow \mathbf{W}^{(\tau-1)} \dots \mathbf{W}^{(0)}$  ▷ forward
  - 3:    $\mathcal{L} \leftarrow \|\text{NN}(\cdot|\theta) - \frac{1}{R} \mathbf{1} \mathbf{1}^\top\|_F^2$  ▷ compute loss
  - 4:   **for all**  $l \in \{0, \dots, \tau - 1\}$  **do** ▷ in parallel
  - 5:      $\widehat{\mathbf{W}}^{(l)} \leftarrow \mathbf{W}^{(l)} \odot \exp(-\eta \nabla_{\mathbf{W}^{(l)}} \mathcal{L})$  ▷ backward
  - 6:      $\widetilde{\mathbf{W}}^{(l)} \leftarrow \widehat{\mathbf{W}}^{(l)} \odot \mathbf{M}^{(l)}$  ▷ enforce sparsity
  - 7:      $\mathbf{W}^{(l)} \leftarrow \mathbf{D}_1^{(l)} \widetilde{\mathbf{W}}^{(l)} \mathbf{D}_2^{(l)}$
  - 8:     ▷ Sinkhorn–Knopp scaling
  - 9:    $\theta \leftarrow \{\mathbf{W}^{(l)}\}_{l=0}^{\tau-1}$  ▷ collecting
- 

(multiplicative) step—preserving nonnegativity—followed by a masked Sinkhorn–Knopp projection [29], [30]—preserving sparsity and imposing double stochasticity. Given the current loss  $\mathcal{L}$ , the updates are

$$\begin{aligned} \widehat{\mathbf{W}}^{(l)} &= \mathbf{W}^{(l)} \odot \exp\left(-\eta \nabla_{\mathbf{W}^{(l)}} \mathcal{L}\right), \\ \widetilde{\mathbf{W}}^{(l)} &= \widehat{\mathbf{W}}^{(l)} \odot \mathbf{M}^{(l)}, \mathbf{W}^{(l)} = \mathbf{D}_1^{(l)} \widetilde{\mathbf{W}}^{(l)} \mathbf{D}_2^{(l)}, \end{aligned} \quad (6)$$

where  $\eta > 0$  is the step size,  $\mathbf{M}^{(l)} \in \{0, 1\}^{R \times R}$  is a mask consistent with  $\mathcal{G}^{(l)}$  that preserves sparsity,  $\mathbf{D}_1^{(l)}, \mathbf{D}_2^{(l)}$  are diagonal matrices that scale rows/columns to make  $\mathbf{W}^{(l)}$  doubly stochastic<sup>1</sup>. Algorithm 1 summarizes the procedure; see the left panel of Fig. 2 for a visual recap.

To produce Figure 3, we choose the step size  $\eta = 8 \times 10^3$ , the maximum iteration  $\mathcal{K} = 3 \times 10^4$ , and uniform initialization  $[0, 1]$  on each  $\mathbf{W}^{(l)}$ , followed by the lazy transform  $\frac{\mathbf{W}^{(l)} + \mathbf{I}}{2}$ .

**Remark 1** (Regarding the total support condition for the masked Sinkhorn–Knopp projection [29]). *The Sinkhorn–Knopp projection onto the set of (masked) doubly stochastic matrices exists, and the alternating normalization converges, if and only if the input nonnegative matrix has total support. In our setting, it suffices to check this property for the mask  $\mathbf{M}^{(l)}$ , since  $\widetilde{\mathbf{W}}^{(l)}$  is strictly positive on the support of  $\mathbf{M}^{(l)}$  and zero elsewhere. In our settings (namely,  $\mathbf{M}^{(l)}$  is symmetric and  $[\mathbf{M}^{(l)}]_{rr} = 1$  for all  $r$ ), every positive entry of  $\mathbf{M}^{(l)}$  lies on a positive diagonal: diagonal entries belong to the identity permutation, and off-diagonal pairs  $(r, q)$  and  $(q, r)$  belong to a permutation that swaps  $r$  and  $q$  while fixing all other indices. Hence  $\mathbf{M}^{(l)}$  has total support, and so does  $\widetilde{\mathbf{W}}^{(l)}$ . It follows that the masked Sinkhorn–Knopp scaling exists,*

1.  $\mathbf{D}_1^{(l)}$  and  $\mathbf{D}_2^{(l)}$  are not a known priori.  $\mathbf{W}^{(l)} = \mathbf{D}_1^{(l)} \widetilde{\mathbf{W}}^{(l)} \mathbf{D}_2^{(l)}$  can be derived by alternating row and column normalizations on  $\widetilde{\mathbf{W}}^{(l)}$ :  $\widetilde{\mathbf{W}}^{(l)} \leftarrow \text{diag}(\widetilde{\mathbf{W}}^{(l)} \mathbf{1})^{-1} \widetilde{\mathbf{W}}^{(l)}$ ,  $\widetilde{\mathbf{W}}^{(l)} \leftarrow \widetilde{\mathbf{W}}^{(l)} \text{diag}(\mathbf{1}^\top \widetilde{\mathbf{W}}^{(l)})^{-1}$ . After a few rounds (or upon convergence), set  $\mathbf{W}^{(l)} \leftarrow \widetilde{\mathbf{W}}^{(l)}$ .

---

**Algorithm 2.** Graph-Aware ATC GT-Diffusion for Decentralized GNSS

**Input:** Mixing matrices  $\theta = \{\mathbf{W}^{(l)}\}_{l=0}^{\tau-1}$  satisfying (2) with entries  $w_{qr}^{(l)}$ ; stepsize  $\mu > 0$ ; maximum iterations  $K$

**Input:** Local data  $\{\mathbf{A}_r, \mathbf{B}_r, \mathbf{Q}_r, \mathbf{y}_r\}_{r=1}^R$  and  $f_r$  as in (4)

**Output:** Estimates  $\{\mathbf{x}_r^K, \mathbf{z}_r^K\}_{r=1}^R$

- 1: **Initialization:** For each node  $r$ , choose  $\mathbf{z}_r^0$  and set  $\mathbf{x}_r^0 \leftarrow (\mathbf{A}_r^\top \mathbf{Q}_r^{-1} \mathbf{A}_r)^{-1} \mathbf{A}_r^\top \mathbf{Q}_r^{-1} (\mathbf{y}_r - \mathbf{B}_r \mathbf{z}_r^0)$ ,  $\mathbf{g}_r^0 \leftarrow \nabla_{\mathbf{z}} f_r(\mathbf{x}_r^0, \mathbf{z}_r^0)$
  - 2: **for**  $k = 0$  **to**  $K - 1$  **do**
  - 3:      $l \leftarrow k \% \tau$                       $\triangleright$  select current topology  $\mathbf{W}^{(l)}$
  - 4:     **for all**  $r \in \{1, \dots, R\}$  **do**                      $\triangleright$  in parallel
  - 5:          $\mathbf{z}_r^{k+1} \leftarrow \sum_{q \in \mathcal{N}_r^{(l)}} w_{qr}^{(l)} (\mathbf{z}_r^k - \mu \mathbf{g}_r^k)$
  - 6:                                      $\triangleright$  adapt + combine state
  - 7:          $\mathbf{x}_r^{k+1} \leftarrow (\mathbf{A}_r^\top \mathbf{Q}_r^{-1} \mathbf{A}_r)^{-1} \mathbf{A}_r^\top \mathbf{Q}_r^{-1} (\mathbf{y}_r - \mathbf{B}_r \mathbf{z}_r^{k+1})$
  - 8:                                      $\triangleright$  local update by exact minimizer
  - 9:          $\mathbf{g}_r^{k+1} \leftarrow \sum_{q \in \mathcal{N}_r^{(l)}} w_{qr}^{(l)} \mathbf{g}_q^k + \nabla_{\mathbf{z}} f_r(\mathbf{x}_r^{k+1}, \mathbf{z}_r^{k+1}) - \nabla_{\mathbf{z}} f_r(\mathbf{x}_r^k, \mathbf{z}_r^k)$       $\triangleright$  combine tracker + gradient tracking
- 

converges and preserves the sparsity pattern (acting blockwise if the mask decomposes).

**Remark 2** (Regarding highly heterogeneous scenarios). It is often desirable to constrain the eigenvalues of  $\mathbf{W}^{(l)}$  to be nonnegative to mitigate large data heterogeneity and to allow for larger step sizes when using the learned  $\theta$  in decentralized optimization, without collapsing the main diagonal entries (zeros will let the smallest eigenvalue hit the negative unity) [27], [31]. A simple way to achieve this is to replace  $\mathbf{W}^{(l)}$  with its lazy version  $\frac{\mathbf{W}^{(l)} + \mathbf{I}}{2}$  in  $\text{NN}(\cdot|\theta)$ , which can be interpreted as adding a residual connection [32] to the deep linear network. A more nuanced approach is to augment the loss with the regularizer  $\Omega(\mathbf{W}^{(l)}) = \|\mathbf{W}^{(l)}\|_* - \text{tr}(\mathbf{W}^{(l)}) = \sum_{r=1}^R (|\lambda_r| - \lambda_r)$ , where  $\lambda_r$  are the eigenvalues of  $\mathbf{W}^{(l)}$ . The trace term  $\text{tr}(\mathbf{W}^{(l)})$  is differentiable, and the nuclear norm  $\|\mathbf{W}^{(l)}\|_*$  is differentiable almost everywhere with gradient  $\frac{\partial \|\mathbf{W}^{(l)}\|_*}{\partial \mathbf{W}^{(l)}} = \mathbf{W}^{(l)} ((\mathbf{W}^{(l)})^\top \mathbf{W}^{(l)})^{-\frac{1}{2}}$  [33] under standard regularity conditions.

### 4.3 Diffusion Algorithm

With  $\theta$ , the Graph-Aware ATC GT-Diffusion algorithm iteratively exchanges the global variable  $\mathbf{z}$  to reach consensus. At iteration  $k$ , each receiver node  $r$  holds  $\mathbf{z}_r^k$  and computes  $\mathbf{x}_r^k = \arg \min_{\mathbf{x}_r} f_r(\mathbf{x}_r | \mathbf{z}_r^k)$ ; using  $\mathbf{x}_r^k$ , the receiver then evaluates  $\nabla_{\mathbf{z}} f_r(\mathbf{x}_r^k, \mathbf{z}_r^k)$ . Aggregating information from neighbors, the Graph-Aware ATC GT-Diffusion updates are:

$$\begin{aligned}
 \mathbf{z}_r^{k+1} &= \sum_{q \in \mathcal{N}_r^{(l)}} w_{qr}^{(l)} (\mathbf{z}_q^k - \mu \mathbf{g}_q^k), \\
 \mathbf{x}_r^{k+1} &= (\mathbf{A}_r^\top \mathbf{Q}_r^{-1} \mathbf{A}_r)^{-1} \mathbf{A}_r^\top \mathbf{Q}_r^{-1} (\mathbf{y}_r - \mathbf{B}_r \mathbf{z}_r^{k+1}), \\
 \mathbf{g}_r^{k+1} &= \sum_{q \in \mathcal{N}_r^{(l)}} w_{qr}^{(l)} \mathbf{g}_q^k + \nabla_{\mathbf{z}} f_r(\mathbf{x}_r^{k+1}, \mathbf{z}_r^{k+1}) - \nabla_{\mathbf{z}} f_r(\mathbf{x}_r^k, \mathbf{z}_r^k),
 \end{aligned} \tag{7}$$

where  $l = k \% \tau$  (i.e.,  $k \bmod \tau$ ),  $\mu > 0$  is the stepsize, and  $\mathbf{g}_r^0 = \nabla_{\mathbf{z}} f_r(\mathbf{x}_r^0, \mathbf{z}_r^0)$ . The tracker  $\mathbf{g}_r^k$  aggregates neighborhood gradients to approximate the centralized gradient; the state  $\mathbf{z}_r^{k+1}$  is updated using this tracked gradient in coordination with neighbors, and then  $\mathbf{x}_r^{k+1}$  is recovered from  $\mathbf{z}_r^{k+1}$  by solving  $\mathbf{x}_r^{k+1} = \arg \min_{\mathbf{x}_r} f_r(\mathbf{x}_r | \mathbf{z}_r^{k+1})$ , as the middle line of (7). The periodic use of the weights  $w_{qr}^{(l)}$  from the sequence  $\theta$  preserves the mixing property in (2), accelerating the consensus of the states and the agreement of the gradient trackers across the network. A high-level implementation is given in Algorithm 2; see also the right panel of Fig. 2.

To produce Figure 4 and Figure 5, we choose a stepsize  $\mu = 0.015$  and limit the number of iterations to  $K = 10^4$ .

**Remark 3** (Analytical reduction). As each update sets  $\mathbf{x}_r^k$  to its exact minimizer, it is convenient for the analysis to eliminate  $\mathbf{x}_r$  and rewrite the local objective  $f_r(\mathbf{x}_r, \mathbf{z})$  solely as a function of  $\mathbf{z}$ :

$$\begin{aligned}
 f_r(\mathbf{z}) &= \frac{1}{2} \|\mathbf{C}_r (\mathbf{B}_r \mathbf{z} - \mathbf{y}_r)\|_{\mathbf{Q}_r^{-1}}^2, \\
 \mathbf{C}_r &\triangleq \mathbf{I} - \mathbf{A}_r (\mathbf{A}_r^\top \mathbf{Q}_r^{-1} \mathbf{A}_r)^{-1} \mathbf{A}_r^\top \mathbf{Q}_r^{-1}.
 \end{aligned} \tag{8}$$

Its gradient w.r.t  $\mathbf{z}$  is therefore

$$\nabla f_r(\mathbf{z}) = \mathbf{B}_r^\top \mathbf{C}_r^\top \mathbf{Q}_r^{-1} \mathbf{C}_r (\mathbf{B}_r \mathbf{z} - \mathbf{y}_r). \tag{9}$$

Note that in implementation,  $\mathbf{x}_r^{k+1}$  is still computed each round as in (7) to evaluate the local gradient and to enable real-time monitoring or enforcement of application-specific quantities that depend on  $\mathbf{x}_r$ .

With Remark 3, let each local vector  $\mathbf{z}_r \in \mathbb{R}^d$ ; an analytical network recursion of (7) can be written compactly as

$$\begin{aligned}
 \mathcal{Z}^{k+1} &= \mathcal{W}^k (\mathcal{Z}^k - \mu \mathcal{G}^k), \\
 \mathcal{G}^{k+1} &= \mathcal{W}^k \mathcal{G}^k + \nabla \mathcal{F}^{k+1} - \nabla \mathcal{F}^k,
 \end{aligned} \tag{10}$$

where the augmented quantities are

$$\begin{aligned}
 \mathcal{Z}^k &\triangleq \text{col}(\mathbf{z}_1^k, \dots, \mathbf{z}_R^k) \in \mathbb{R}^{Rd}, \\
 \mathcal{G}^k &\triangleq \text{col}(\mathbf{g}_1^k, \dots, \mathbf{g}_R^k) \in \mathbb{R}^{Rd}, \\
 \mathcal{W}^k &\triangleq \mathbf{W}^{(k \% \tau)} \otimes \mathbf{I}_d \in \mathbb{R}^{Rd \times Rd}, \\
 \nabla \mathcal{F}^k &\triangleq \text{col}(\nabla f_1(\mathbf{z}_1^k), \dots, \nabla f_R(\mathbf{z}_R^k)) \in \mathbb{R}^{Rd}.
 \end{aligned} \tag{11}$$

In addition, define the network averages (centroids) of  $\mathcal{Z}^k$ ,  $\mathcal{G}^k$ , and  $\nabla \mathcal{F}^k$  as

$$\begin{aligned}
 \bar{\mathbf{z}}^k &\triangleq \frac{1}{R} \sum \mathbf{z}_r^k = \frac{1}{R} (\mathbf{1}^\top \otimes \mathbf{I}_d) \mathcal{Z}^k \in \mathbb{R}^d, \\
 \bar{\mathbf{g}}^k &\triangleq \frac{1}{R} \sum \mathbf{g}_r^k = \frac{1}{R} (\mathbf{1}^\top \otimes \mathbf{I}_d) \mathcal{G}^k \in \mathbb{R}^d, \\
 \bar{\nabla} f^k &\triangleq \frac{1}{R} \sum \nabla f_r(\mathbf{z}_r^k) = \frac{1}{R} (\mathbf{1}^\top \otimes \mathbf{I}_d) \nabla \mathcal{F}^k \in \mathbb{R}^d.
 \end{aligned} \tag{12}$$

These compact expressions will be vital for the convergence analysis.

## 5 SUPPLEMENTARY NOTE 1: PROOF OF LINEAR CONVERGENCE FOR GRAPH-AWARE ATC GT-DIFFUSION

In this note, we present a gentle and self-contained convergence analysis of the proposed Graph-Aware ATC GT-Diffusion algorithm, tailored to the GNSS setting. The development proceeds in three steps: (i) we state the convergence target and assumptions; (ii) we derive the key error recursions and supporting lemmas; and (iii) we establish the main linear-convergence result and discuss the associated trade-offs and parameter choices.

### 5.1 Necessary Assumptions

The analysis of (10) aims to show that  $\mathcal{Z}^k \rightarrow \mathbf{1} \otimes \mathbf{z}^*$  as  $k \rightarrow \infty$  (under suitable norms, for example MSD  $\|\mathcal{Z}^k - \mathbf{1} \otimes \mathbf{z}^*\|^2/R$ ), where  $\mathbf{z}^*$  denotes the centralized minimizer. We base our analysis on a standard GT framework within the smooth and strongly convex regime, which allows us to characterize convergence rates in terms of condition numbers. The standing assumptions are formalized below.

**Assumption 1** (Strong convexity and smoothness). *Each local loss function  $f_r(\mathbf{z})$  from (8) is  $L$ -smooth with  $L = \sup_r \lambda_{\max}(\mathbf{H}_r)$  and Hessian  $\mathbf{H}_r = \nabla^2 f_r(\mathbf{z}) \succeq \mathbf{0}$ . The global objective  $F(\mathbf{z}) = \frac{1}{R} \sum_{r=1}^R f_r(\mathbf{z})$  is  $m$ -strongly convex with  $m = \lambda_{\min}(\mathbf{H})$  and aggregate Hessian  $\mathbf{H} = \frac{1}{R} \sum_{r=1}^R \mathbf{H}_r \succ \mathbf{0}$ .  $Q = L/m \geq 1$  is the condition number.*

**Assumption 2** (Block contraction over  $\tau$  steps). *For all  $l$ ,  $\mathbf{W}^{(l)}$  is doubly stochastic (i.e.,  $\mathbf{W}^{(l)}\mathbf{1} = \mathbf{1}$ ,  $\mathbf{1}^\top \mathbf{W}^{(l)} = \mathbf{1}^\top$ ) and respects the sparsity pattern of  $\mathcal{G}^{(l)}$ . There exists  $\epsilon_\tau \in (0, 1)$  such that  $\|\mathbf{W}^{(\tau-1)} \dots \mathbf{W}^{(0)} - \frac{1}{R} \mathbf{1}\mathbf{1}^\top\| = \epsilon_\tau$  as in (2).*

### 5.2 Error Recursion and Lemmas

Rather than working directly with the limit  $\mathcal{Z}^k \rightarrow \mathbf{1} \otimes \mathbf{z}^*$ , we introduce the consensus projector  $\mathcal{J} = \frac{1}{R} (\mathbf{1}\mathbf{1}^\top) \otimes \mathbf{I}_d \in \mathbb{R}^{Rd \times Rd}$  and its orthogonal complement  $\mathcal{J}_\perp = \mathbf{I}_{Rd} - \mathcal{J} \in \mathbb{R}^{Rd \times Rd}$ , and define the error quantities:

$$\begin{aligned} \mathcal{C}^k &= \mathcal{J}_\perp \mathcal{Z}^k, & \mathcal{T}^k &= \mathcal{J}_\perp G^k, \\ \mathbf{s}^k &= \bar{\mathbf{z}}^k - \mathbf{z}^* & \text{and} & \quad \Delta^k = \bar{\mathbf{g}}^k - \nabla F(\bar{\mathbf{z}}^k). \end{aligned} \quad (13)$$

Here,  $\mathcal{C}^k$  (**network disagreement**) measures deviation from the consensus subspace;  $\mathcal{C}^k = \mathbf{0}$  iff all agents share the same iterate.  $\mathcal{T}^k$  (tracking disagreement) measures disagreement among gradient trackers;  $\mathcal{T}^k = \mathbf{0}$  iff the trackers are consensual.  $\mathbf{s}^k$  (average optimality error) vanishes iff the network average equals the optimizer  $\mathbf{z}^*$ .  $\Delta^k$  (inexact gradient error) is the bias of  $\bar{\mathbf{g}}^k$  (**averaged gradient**) at  $\bar{\mathbf{z}}^k$ ;  $\Delta^k = \mathbf{0}$  under exact tracking or noise-free gradients.

With these notations, convergence to a consensual optimizer is equivalent to the joint vanishing of the errors. Under suitable norms, we have

$$\mathcal{C}^k \rightarrow \mathbf{0}, \quad \mathcal{T}^k \rightarrow \mathbf{0}, \quad \mathbf{s}^k \rightarrow \mathbf{0} \quad \text{as } (k \rightarrow \infty), \quad (14)$$

in the presence of gradient error  $\Delta^k$ . Based on this understanding, we derive the following lemmas.

**Lemma 1** (Average identities). *Under Assumption 1–2, the following hold for all  $k \geq 0$ :*

$$\bar{\mathbf{z}}^{k+1} = \bar{\mathbf{z}}^k - \mu \bar{\mathbf{g}}^k, \quad (15)$$

$$\bar{\mathbf{g}}^{k+1} = \bar{\mathbf{g}}^k + \overline{\nabla f}^{k+1} - \overline{\nabla f}^k = \overline{\nabla f}^{k+1}. \quad (16)$$

Moreover, it follows that

$$\begin{aligned} \|\Delta^k\| &= \left\| \overline{\nabla f}^k - \nabla F(\bar{\mathbf{z}}^k) \right\| \\ &= \left\| \frac{1}{R} \sum_{r=1}^R (\nabla f_r(\mathbf{z}_r^k) - \nabla f_r(\bar{\mathbf{z}}^k)) \right\| \leq \frac{L}{\sqrt{R}} \|\mathcal{C}^k\|. \end{aligned} \quad (17)$$

*Proof.* See Appendix A.  $\square$

**Lemma 2** (Average descent). *Under Assumption 1, for any  $\mu \in (0, 1/L]$ , we have*

$$\|\mathbf{s}^{k+1}\| \leq (1 - m\mu) \|\mathbf{s}^k\| + \mu \|\Delta^k\| \leq \alpha_1 \|\mathbf{s}^k\| + \alpha_2 \|\mathcal{C}^k\|, \quad (18)$$

where  $\alpha_1 = 1 - m\mu$  and  $\alpha_2 = \mu \frac{L}{\sqrt{R}}$ .

*Proof.* See Appendix B.  $\square$

Lemma 1 states that in our Graph-Aware ATC GT-Diffusion, the centroids  $(\bar{\mathbf{z}}^k, \bar{\mathbf{g}}^k)$  evolve like a centralized update on  $F(\mathbf{z})$  but with a perturbation. The only difference is that the global gradient at the average,  $\nabla F(\bar{\mathbf{z}}^k)$ , is replaced by the network-average gradient  $\overline{\nabla f}^k$ . The resulting bias is precisely  $\Delta^k$ , and (17) shows that its norm is upper bounded by the scaled disagreement norm  $\|\mathcal{C}^k\|$ . Building on this, Lemma 2 establishes that, under the centroid dynamics of Lemma 1, the average optimality error  $\|\mathbf{s}^k\|$  contracts by a factor  $\alpha_1$  up to an additive term  $\alpha_2 \|\mathcal{C}^k\|$ . Therefore, it remains to show that  $\|\mathcal{C}^k\|$  also decreases. We now analyze the dynamics of the disagreement  $\mathcal{C}^k$ .

**Lemma 3** (Network disagreement recursion). *For recursion over window period  $\{(i-1)\tau, \dots, k-1, k\}$  where  $k \in \mathcal{I}_i = \{i\tau, \dots, (i+1)\tau - 1\}$ , the network disagreement  $\mathcal{C}^k$  satisfies*

$$\|\mathcal{C}^k\| \leq \epsilon_\tau \|\mathcal{C}^{(i-1)\tau}\| + \mu \sum_{j=(i-1)\tau}^{k-1} \|\mathcal{T}^j\|. \quad (19)$$

*Proof.* See Appendix C.  $\square$

**Lemma 4** (Tracking error recursion). *For recursion over window period  $\{(i-1)\tau, \dots, k-1, k\}$ , where  $k \in \mathcal{I}_i = \{i\tau, \dots, (i+1)\tau-1\}$ , the tracking disagreement  $\mathcal{T}^k$  satisfies*

$$\begin{aligned} \|\mathcal{T}^k\| &\leq \epsilon_\tau \|\mathcal{T}^{(i-1)\tau}\| + \beta_1 \sum_{j=(i-1)\tau}^{k-1} \|\mathcal{C}^j\| + \beta_2 \sum_{j=(i-1)\tau}^{k-1} \|\mathcal{T}^j\| \\ &\quad + \beta_3 \sum_{j=(i-1)\tau}^{k-1} \|\mathbf{s}^j\|, \end{aligned} \quad (20)$$

where

$$\begin{aligned} \beta_1 &= L c_W + \mu L^2, \quad \beta_2 = \mu L, \\ \beta_3 &= \mu \sqrt{R} L^2, \quad c_W = \sup_j \|(\mathbf{W}^{(j\% \tau)} - \mathbf{I})\|_{\mathcal{J}_\perp} \leq 2. \end{aligned} \quad (21)$$

*Proof.* See Appendix D.  $\square$

Instead of analyzing single iterations, Lemmas 3 and 4 study a block iterate that spans one full period of the mixing combination matrices, as specified in Assumption 2, where per-iteration graph connectivity may fail. These lemmas show that, although Assumption 2 guarantees a block-wise contraction between the beginning and end of each period, it also introduces summations across the intermediate steps within the block, complicating the analysis. Consequently, the standard small-increment argument is impractical, and the sections that follow develop an alternative analysis framework tailored to this setting.

### 5.3 Convergence Results

We define  $T_i = \max_{k \in \mathcal{I}_i} \|\mathcal{T}^k\|$ ,  $C_i = \max_{k \in \mathcal{I}_i} \|\mathcal{C}^k\|$ ,  $S_i = \max_{k \in \mathcal{I}_i} \|\mathbf{s}^k\|$ . Lemma 4 can therefore be expressed as

$$\begin{aligned} T_i &\leq \epsilon_\tau T_{i-1} + \tau \beta_1 C_{i-1} + (\tau-1)\beta_1 C_i + \tau \beta_2 T_{i-1} \\ &\quad + (\tau-1)\beta_2 T_i + \tau \beta_3 S_{i-1} + (\tau-1)\beta_3 S_i, \end{aligned} \quad (22)$$

with  $\max_{k \in \mathcal{I}_i} \|\mathcal{T}^{(i-1)\tau}\| \leq T_{i-1}$ , and

$$\begin{aligned} &\max_{k \in \mathcal{I}_i} \sum_{j=(i-1)\tau}^{k-1} \|\mathcal{C}^j\| \\ &\leq \max_{k \in \mathcal{I}_i} \sum_{j=(i-1)\tau}^{i\tau-1} \|\mathcal{C}^j\| + \max_{k \in \mathcal{I}_i} \sum_{j=i\tau}^{k-1} \|\mathcal{C}^j\| \\ &\leq \sum_{j=(i-1)\tau}^{i\tau-1} C_{i-1} + \max_{k \in \mathcal{I}_i} \sum_{j=i\tau}^{(i+1)\tau-2} \|\mathcal{C}^j\| \leq \tau C_{i-1} + (\tau-1)C_i \end{aligned} \quad (23)$$

(same for  $\max_{k \in \mathcal{I}_i} \sum_{j=(i-1)\tau}^{k-1} \{\|\mathcal{T}^j\|, \|\mathbf{s}^j\|\}$ ). Lemma 3 is

$$C_i \leq \epsilon_\tau C_{i-1} + \tau \mu T_{i-1} + (\tau-1)\mu T_i, \quad (24)$$

and Lemma 2 can be rewritten as

$$\begin{aligned} S_i &\leq \alpha_1^\tau S_{i-1} + \tau \alpha_2 C_{i-1} + (\tau-1)\alpha_2 C_i \\ &\leq (1 - \frac{m\tau}{2}\mu) + \tau \alpha_2 C_{i-1} + (\tau-1)\alpha_2 C_i \end{aligned} \quad (25)$$

for  $\mu \leq \frac{1}{m\tau}$ . Moreover, with  $\mathbf{v}_i = [c_W \tau C_i, L^{-1} T_i, \sqrt{R} S_i]^\top$ , we can equivalently express (22), (24) and (25) as

$$\begin{aligned} \mathbf{v}_i &\leq \left( \underbrace{\begin{bmatrix} \epsilon_\tau & 0 & 0 \\ 1 & \epsilon_\tau & 0 \\ 0 & 0 & 1 \end{bmatrix}}_{\boldsymbol{\varphi}_0} + \underbrace{\begin{bmatrix} 0 & c_W \tau & 0 \\ \frac{1}{c_W \tau} & 1 & 1 \\ \frac{1}{c_W \tau} & 0 & \frac{1}{2Q} \end{bmatrix}}_{\boldsymbol{\varphi}_1} \tau L \mu \right) \mathbf{v}_{i-1} \\ &\quad + \left( \underbrace{\begin{bmatrix} 0 & 0 & 0 \\ 1 - \frac{1}{\tau} & 0 & 0 \\ 0 & 0 & 0 \end{bmatrix}}_{\boldsymbol{\psi}_0} + \underbrace{\begin{bmatrix} 0 & c_W \tau & 0 \\ \frac{1}{c_W \tau} & 1 & 1 \\ \frac{1}{c_W \tau} & 0 & 0 \end{bmatrix}}_{\boldsymbol{\psi}_1} (\tau-1) L \mu \right) \mathbf{v}_i. \end{aligned} \quad (26)$$

Let  $\omega = L\mu < 1$ , (26) can be further written as

$$\mathbf{v}_i \leq (\mathbf{I} - \boldsymbol{\psi}_0 - \boldsymbol{\psi}_1(\tau-1)\omega)^{-1} (\boldsymbol{\varphi}_0 + \boldsymbol{\varphi}_1 \tau \omega) \mathbf{v}_{i-1}, \quad (27)$$

provided that  $\mathbf{I} - \boldsymbol{\psi}_0 - \boldsymbol{\psi}_1(\tau-1)\omega$  is invertible. To streamline notations, we introduce

$$\begin{aligned} \mathcal{H}(\omega) &= \mathcal{R}(\omega) \boldsymbol{\varphi}(\omega), \quad \mathcal{R}(\omega) = (\mathbf{I} - \boldsymbol{\psi}(\omega))^{-1}, \\ \boldsymbol{\psi}(\omega) &= \boldsymbol{\psi}_0 + \boldsymbol{\psi}_1(\tau-1)\omega, \quad \boldsymbol{\varphi}(\omega) = \boldsymbol{\varphi}_0 + \boldsymbol{\varphi}_1 \tau \omega, \end{aligned} \quad (28)$$

and represent (27) by  $\mathbf{v}_i \leq \mathcal{H}(\omega) \mathbf{v}_{i-1}$ , thus indicating that convergence holds if the spectral radius  $\rho(\mathcal{H}(\omega)) < 1$ . However, the complexity of  $\mathcal{H}(\omega)$  makes  $\rho(\mathcal{H}(\omega))$  less explicit, and often challenging to derive since it departs from classical, non-recursive small-gain framework. Consequently, the standard analytical tools do not apply in the present setting. Alternatively, we adopt matrix perturbation theory [34] for our analysis as follows.

**Theorem 1** (Simple eigenvalue perturbation, restated in our notation [34]–[36]). *Let  $\mathcal{H}(\omega)$  be analytic around  $\omega_0$ ,  $\mathcal{H}(\omega_0)$  has a simple eigenvalue  $\lambda_0$  with left/right eigenvectors  $\mathbf{l}_0^*$ ,  $\mathbf{r}_0$  normalized by  $\mathbf{l}_0^* \mathbf{r}_0 = 1$ , then there exists analytic maps  $\lambda(\omega)$ ,  $\mathbf{l}^*(\omega)$ ,  $\mathbf{r}(\omega)$  that establish  $\mathbf{l}^*(\omega) \mathcal{H}(\omega) = \lambda(\omega) \mathbf{l}^*(\omega)$ ,  $\mathcal{H}(\omega) \mathbf{r}(\omega) = \lambda(\omega) \mathbf{r}(\omega)$  and  $\mathbf{l}^*(\omega) \mathbf{r}(\omega) = 1$  with initial condition  $\lambda(\omega_0) = \lambda_0$ ,  $\mathbf{l}^*(\omega_0) = \mathbf{l}_0^*$ ,  $\mathbf{r}(\omega_0) = \mathbf{r}_0$ . And the derivatives hold*

$$\begin{aligned} \lambda'(\omega) &= \mathbf{l}^*(\omega) \mathcal{H}'(\omega) \mathbf{r}(\omega), \\ \lambda''(\omega) &= \mathbf{l}^*(\omega) \mathcal{H}''(\omega) \mathbf{r}(\omega) - 2\mathbf{l}^*(\omega) \mathcal{H}'(\omega) \mathcal{S}(\omega) \mathcal{H}'(\omega) \mathbf{r}(\omega), \\ \lambda'''(\omega) &= \mathbf{l}^*(\omega) \mathcal{H}'''(\omega) \mathbf{r}(\omega) \\ &\quad - 3\mathbf{l}^*(\omega) \left( \mathcal{H}''(\omega) \mathcal{S}(\omega) \mathcal{H}'(\omega) + \mathcal{H}'(\omega) \mathcal{S}(\omega) \mathcal{H}''(\omega) \right) \mathbf{r}(\omega) \\ &\quad + 6\mathbf{l}^*(\omega) \mathcal{H}'(\omega) \mathcal{S}(\omega) \left( \mathcal{H}'(\omega) - \lambda'(\omega) \mathbf{I} \right) \mathcal{S}(\omega) \mathcal{H}'(\omega) \mathbf{r}(\omega), \end{aligned} \quad (29)$$

where  $\mathcal{S}(\omega)$  satisfies

$$\begin{aligned} (\mathcal{H}(\omega) - \lambda(\omega) \mathbf{I}) \mathcal{S}(\omega) &= \mathcal{S}(\omega) (\mathcal{H}(\omega) - \lambda(\omega) \mathbf{I}) = \mathbf{I} - \mathcal{P}(\omega), \\ \mathcal{P}(\omega) &= \mathbf{r}(\omega) \mathbf{l}^*(\omega), \quad \mathcal{S}(\omega) \mathbf{r}(\omega) = 0, \quad \mathbf{l}^*(\omega) \mathcal{S}(\omega) = 0. \end{aligned} \quad (30)$$

**Definition 1** (Riesz projection and reduced resolvent [36], [37]). *Let  $\Gamma$  be a simple closed contour in the complex plane that*

encloses the eigenvalue  $\lambda(\omega)$  of  $\mathcal{H}(\omega)$  and no other eigenvalues. Then the operators  $\mathcal{P}(\omega)$  and  $\mathcal{S}(\omega)$  from (30) in Theorem 1 can be equivalently written as

$$\begin{aligned}\mathcal{P}(\omega) &= -\frac{1}{2\pi j} \oint_{\Gamma} (\mathcal{H}(\omega) - z\mathbf{I})^{-1} dz, \\ \mathcal{S}(\omega) &= \frac{1}{2\pi j} \oint_{\Gamma} \frac{1}{\lambda(\omega) - z} (\mathcal{H}(\omega) - z\mathbf{I})^{-1} dz,\end{aligned}\quad (31)$$

where  $\mathcal{P}(\omega)$  is the Riesz projection associated with  $\lambda(\omega)$  and  $\mathcal{S}(\omega)$  is the corresponding reduced resolvent.

Theorem 1 restates the classical Stewart–Sun/Kato results, giving explicit derivatives for a simple eigenvalue  $\lambda(\omega)$  of an analytic matrix function  $\mathcal{H}(\omega)$  regardless of its complexity. Definition 1 complements this by expressing the key operators, the Riesz projection  $\mathcal{P}(\omega)$  and reduced resolvent  $\mathcal{S}(\omega)$ , as contour integrals. These analytic representations are crucial, as they allow us to use contour integration techniques to bound the norms of these operators, which in turn enables the derivation of computable bounds on the motion of the spectral radius  $\rho(\mathcal{H}(\omega))$ .

Furthermore, we derive constants bounding the relative norms of  $\{\psi_0, \psi_1, \varphi_0, \varphi_1\}$

$$\begin{aligned}c_1 &= 2 - 1/\tau \geq \|(\mathbf{I} - \psi_0)^{-1}\|_{\infty}, \\ c_2 &= (2\tau + 1)(\tau - 1) \geq \|(\mathbf{I} - \psi_0)^{-1}\psi_1(\tau - 1)\|_{\infty}, \\ c_3 &= 1 + \epsilon_{\tau} \geq \|\varphi_0\|_{\infty}, \quad c_4 = 2\tau + 1 \geq \|\varphi_1\|_{\infty};\end{aligned}\quad (32)$$

together with composite constants

$$\begin{aligned}c_{\mathcal{P}} &= 2 + 4\frac{1 + \epsilon_{\tau}}{1 - \epsilon_{\tau}}, \quad c_{\mathcal{S}} = \frac{4}{1 - \epsilon_{\tau}} c_{\mathcal{P}}, \\ c_{\mathcal{H}'} &= 2c_1(c_2c_3 + \tau c_4) \left( \frac{2}{1 - \epsilon_{\tau}} + \frac{4(1 + \epsilon_{\tau})}{(1 - \epsilon_{\tau})^2} \right), \\ K_3 &= c_{\mathcal{P}} \left( 19c_1c_2^2(c_2c_3 + \tau c_4) + 60c_{\mathcal{S}}c_1^2c_2(c_2c_3 + \tau c_4)^2 \right. \\ &\quad \left. + 48c_{\mathcal{S}}^2(1 + c_{\mathcal{P}})c_1^3(c_2c_3 + \tau c_4)^3 \right),\end{aligned}\quad (33)$$

whose precise roles will be given in the subsequent section, as preparation for the convergence result that follows.

**Theorem 2** (The linear convergence of: *Graph-Aware ATC GT-Diffusion*). *Let Assumptions 1 and 2 hold, together with constant sets (32) (33). If the stepsize  $\mu$  in ATC GT-Diffusion satisfies*

$$\mu \leq \min \left\{ \frac{1}{\tau m}, \frac{1}{4c_2L}, \frac{1}{2c_{\mathcal{H}'}L}, \frac{1}{L} \sqrt{\frac{3\tau}{2QK_3}} \right\}.\quad (34)$$

then there exists  $\varrho > 0$  such that

$$C_i + T_i + S_i \leq \varrho \left( 1 - \frac{m\tau}{4} \mu \right)^i (C_0 + T_0 + S_0) \quad \text{for all } i \geq 0.\quad (35)$$

Consequently,  $\|C^k\| \rightarrow 0$ ,  $\|T^k\| \rightarrow 0$ , and  $\|S^k\| \rightarrow 0$ , the global state  $Z^k$  converges to the exact minimizer  $\mathbf{1} \otimes \mathbf{z}^*$  linearly.

*Proof.* The proof begins by expanding  $\mathcal{H}(\omega)$  around  $\omega_0 = 0$  to establish convergence for sufficiently small stepsizes. By having  $\omega_0 = 0$  in (26) (27), we derive

$$\mathcal{H}(0) = \begin{bmatrix} \epsilon_{\tau} & 0 & 0 \\ 1 + (1 - \frac{1}{\tau})\epsilon_{\tau} & \epsilon_{\tau} & 0 \\ 0 & 0 & 1 \end{bmatrix}.\quad (36)$$

As  $\mathcal{H}(0)$  is a lower triangular matrix, we find  $\{\epsilon_{\tau}, \epsilon_{\tau}, 1\}$  form its eigenvalues, and 1 is the simple eigenvalue that also dominates the spectral radius ( $\epsilon_{\tau} < 1$ ). In addition, 1's corresponding eigenvector is as simple as  $\mathbf{e}_3 = [0, 0, 1]^{\top}$ . By Theorem 1, perturbations  $\lambda(\omega), \mathbf{l}^*(\omega), \mathbf{r}(\omega)$  with initialization  $\lambda_0 = 1, \mathbf{l}_0 = \mathbf{r}_0 = \mathbf{e}_3$  can be analyzed as the characterization of spectral radius motions of  $\mathcal{H}(\omega)$ . Specifically, we derive the point eigenvalue derivative

$$\begin{aligned}\lambda'(0) &= \mathbf{l}_0^* \mathcal{H}'(0) \mathbf{r}_0 = \mathbf{e}_3^{\top} \mathcal{H}'(0) \mathbf{e}_3 = \frac{-\tau}{2Q}, \\ \lambda''(0) &= \mathbf{l}_0^* \mathcal{H}''(0) \mathbf{r}_0 - 2\mathbf{l}_0^* \mathcal{H}'(0) \mathcal{S}(0) \mathcal{H}'(0) \mathbf{r}_0 = 0,\end{aligned}\quad (37)$$

by exploiting differentials

$$\begin{aligned}\mathcal{H}'(\omega) &= \mathcal{R}(\omega) (\psi'(\omega) \mathcal{R}(\omega) \varphi(\omega) + \varphi'(\omega)), \\ \mathcal{H}''(\omega) &= 2\mathcal{R}(\omega) \psi'(\omega) \mathcal{R}(\omega) (\psi'(\omega) \mathcal{R}(\omega) \varphi(\omega) + \varphi'(\omega)), \\ \mathcal{H}'''(\omega) &= 6(\mathcal{R}(\omega) \psi'(\omega))^2 \mathcal{R}(\omega) (\psi'(\omega) \mathcal{R}(\omega) \varphi(\omega) + \varphi'(\omega)),\end{aligned}\quad (38)$$

at  $\omega_0 = 0$  and combining (30) with

$$\mathcal{S}(0) = \begin{bmatrix} \frac{1}{\epsilon_{\tau}-1} & 0 & 0 \\ \frac{-1 - (1 - \frac{1}{\tau})\epsilon_{\tau}}{(\epsilon_{\tau}-1)^2} & \frac{1}{\epsilon_{\tau}-1} & 0 \\ 0 & 0 & 0 \end{bmatrix}.\quad (39)$$

Then, by Taylor expansion at  $\omega_0 = 0$ , it holds

$$\begin{aligned}\lambda(\omega) &= \lambda(0) + \lambda'(0)\omega + \frac{\lambda''(0)}{2}\omega^2 + \frac{\lambda'''(\xi)}{6}\omega^3 \\ &= 1 - \frac{\tau}{2Q}\omega + \frac{\lambda'''(\xi)}{6}\omega^3, \quad \text{for } 0 < \xi \leq \omega.\end{aligned}\quad (40)$$

As we can see, (40) tells an unachievable maximum rate  $1 - \frac{\tau}{2Q}\omega$  with a remainder  $\frac{\lambda'''(\xi)}{6}\omega^3$  if  $\lambda(\omega)$  dominates the radius by  $|\lambda(\omega)| = \rho(\mathcal{H}(\omega))$ . To bound  $\lambda(\omega)$ 's motion, we need the remainder to be absorbed, and it holds

$$\begin{aligned}|\lambda'''(\xi)| &\leq \left| \mathbf{l}^*(\xi) \mathcal{H}'''(\xi) \mathbf{r}(\xi) \right. \\ &\quad \left. - 3\mathbf{l}^*(\xi) \left( \mathcal{H}''(\xi) \mathcal{S}(\xi) \mathcal{H}'(\xi) + \mathcal{H}'(\xi) \mathcal{S}(\xi) \mathcal{H}''(\xi) \right) \mathbf{r}(\xi) \right. \\ &\quad \left. + 6\mathbf{l}^*(\xi) \mathcal{H}'(\xi) \mathcal{S}(\xi) \left( \mathcal{H}'(\xi) - \lambda'(\xi) \mathbf{I} \right) \mathcal{S}(\xi) \mathcal{H}'(\xi) \mathbf{r}(\xi) \right| \\ &\leq \|\mathcal{P}(\xi)\|_{\infty} \left( \|\mathcal{H}'''(\xi)\|_{\infty} \right. \\ &\quad \left. + 6\|\mathcal{H}''(\xi)\|_{\infty} \|\mathcal{S}(\xi)\|_{\infty} \|\mathcal{H}'(\xi)\|_{\infty} \right. \\ &\quad \left. + 6(1 + \|\mathcal{P}(\xi)\|_{\infty}) \|\mathcal{S}(\xi)\|_{\infty}^2 \|\mathcal{H}'(\xi)\|_{\infty}^3 \right),\end{aligned}\quad (41)$$

where the second inequality is based on  $|\mathbf{l}^*(\xi)(\cdot)\mathbf{r}(\xi)| \leq \|\mathcal{P}(\xi)\|_{\infty} \|(\cdot)\|_{\infty}$  and  $\lambda'(\xi) = \mathbf{l}^*(\xi) \mathcal{H}'(\xi) \mathbf{r}(\xi)$ . As we can

see, several quantities ( $\|\mathcal{H}'(\xi)\|_\infty, \|\mathcal{H}''(\xi)\|_\infty, \|\mathcal{H}'''(\xi)\|_\infty, \|\mathcal{P}(\xi)\|_\infty$  and  $\|\mathcal{S}(\xi)\|_\infty$ ) are needed for (41). From the relations in (28) and (38), one can derive  $\|\mathcal{R}(\xi)\|_\infty$  as preparation for  $\|\mathcal{H}'(\xi)\|_\infty, \|\mathcal{H}''(\xi)\|_\infty, \|\mathcal{H}'''(\xi)\|_\infty$ . Let  $\xi \leq \omega \leq \frac{1}{4c_2}$  (the second term in (34) appears),  $\mathbf{I} - \psi(\omega)$  is invertible and  $\mathcal{R}(\xi)$  can be bounded

$$\begin{aligned} \|\mathcal{R}(\xi)\|_\infty &\leq \|(\mathbf{I} - \psi_0)^{-1}\|_\infty \|\mathbf{I} - (\mathbf{I} - \psi_0)^{-1} \psi_1(\tau - 1)\xi\|_\infty \\ &\leq c_1 \frac{1}{1 - c_2\xi} \leq \frac{4}{3}c_1 \end{aligned} \quad (42)$$

where the second inequality is based on the Neumann series sum over  $\xi$  and consolidating constants via (32). Under (42), it further establishes

$$\begin{aligned} \|\mathcal{H}'(\xi)\|_\infty &\leq \frac{c_1}{(1 - c_2\xi)^2} (c_2c_3 + \tau c_4) \leq 2c_1(c_2c_3 + \tau c_4), \\ \|\mathcal{H}''(\xi)\|_\infty &\leq \frac{2c_1c_2}{(1 - c_2\xi)^3} (c_2c_3 + \tau c_4) \leq 5c_1c_2(c_2c_3 + \tau c_4), \\ \|\mathcal{H}'''(\xi)\|_\infty &\leq \frac{6c_1c_2^2}{(1 - c_2\xi)^4} (c_2c_3 + \tau c_4) \leq 19c_1c_2^2(c_2c_3 + \tau c_4), \end{aligned} \quad (43)$$

by substituting into (38), invoking the norm's subadditivity and submultiplicativity, and consolidating constants similar to (42). Subsequently, it remains to derive  $\|\mathcal{P}(\xi)\|_\infty$  and  $\|\mathcal{S}(\xi)\|_\infty$  for the final bound on (41). Let  $g = 1 - \epsilon_\tau$  be spectral gap of eigenvalue set  $\{\epsilon_\tau, \epsilon_\tau, 1\}$  from  $\mathcal{H}(0)$  and set a contour  $\Gamma : |z - 1| = g/2$ , the resolvent

$$\begin{aligned} &\sup_{z \in \Gamma} \|(\mathcal{H}(0) - z\mathbf{I})^{-1}\|_\infty \\ &= \sup_{z \in \Gamma} \left\| \begin{bmatrix} \frac{1}{z - \epsilon_\tau} & 0 & 0 \\ \frac{-1 - (1 - \frac{1}{2})\epsilon_\tau}{(z - \epsilon_\tau)^2} & \frac{1}{z - \epsilon_\tau} & 0 \\ 0 & 0 & \frac{1}{z - 1} \end{bmatrix} \right\|_\infty \leq \frac{2}{g} + \frac{4(1 + \epsilon_\tau)}{g^2}. \end{aligned} \quad (44)$$

By introducing  $\Delta(\xi) = \mathcal{H}(\xi) - \mathcal{H}(0)$ , it holds

$$\begin{aligned} &\sup_{z \in \Gamma} \|(\mathcal{H}(\xi) - z\mathbf{I})^{-1}\|_\infty \\ &= \sup_{z \in \Gamma} \left\| (\mathbf{I} + (\mathcal{H}(0) - z\mathbf{I})^{-1} \Delta(\xi))^{-1} (\mathcal{H}(0) - z\mathbf{I})^{-1} \right\|_\infty. \end{aligned} \quad (45)$$

Let  $\xi \leq \omega \leq \frac{1}{2c_{\mathcal{H}'}}$  (the third term in (34) appears), Neumann smallness condition holds:

$$\begin{aligned} &\sup_{z \in \Gamma} \|(\mathcal{H}(0) - z\mathbf{I})^{-1}\|_\infty \|\Delta(\xi)\|_\infty \\ &\leq \left( \frac{2}{g} + \frac{4(1 + \epsilon_\tau)}{g^2} \right) \|\mathcal{H}'(\xi)\|_\infty \frac{1}{2c_{\mathcal{H}'}} \leq \frac{1}{2}, \end{aligned} \quad (46)$$

where the first inequality is based on the mean value theorem on  $\Delta(\xi)$  and (33) (43) (44). Here,  $c_{\mathcal{H}'}$  appears as the separation guarantee for the spectrum. Hence, (45) can be rewritten as

$$\sup_{z \in \Gamma} \|(\mathcal{H}(\xi) - z\mathbf{I})^{-1}\|_\infty \leq 2 \left( \frac{2}{g} + \frac{4(1 + \epsilon_\tau)}{g^2} \right). \quad (47)$$

By (47), the resolvent is well-defined on  $\Gamma$ , so exactly one eigenvalue  $\lambda(\omega)$  of  $\mathcal{H}(\omega)$  lies in the disk of  $\Gamma$ . One can check

$\Gamma_\epsilon : |z - \epsilon_\tau| = g/2$  traps the other two eigenvalues within the  $\Gamma_\epsilon$  under the same condition. Hence  $|\lambda(\omega)| = \rho(\mathcal{H}(\omega))$ , which justifies the initial statement. By Definition 1, we have

$$\begin{aligned} &\|\mathcal{P}(\xi)\|_\infty \\ &\leq \frac{1}{2\pi} \int_\Gamma \|(\mathcal{H}(\xi) - z\mathbf{I})^{-1}\|_\infty |dz| \\ &\leq \frac{g}{2} \cdot \sup_{z \in \Gamma} \|(\mathcal{H}(\xi) - z\mathbf{I})^{-1}\|_\infty \leq 2 + 4 \frac{1 + \epsilon_\tau}{1 - \epsilon_\tau} = c_{\mathcal{P}}, \end{aligned} \quad (48)$$

$$\begin{aligned} &\|\mathcal{S}(\xi)\|_\infty \\ &\leq \frac{1}{2\pi} \int_\Gamma \frac{1}{|\lambda(\xi) - z|} \|(\mathcal{H}(\xi) - z\mathbf{I})^{-1}\|_\infty |dz| \\ &\leq \frac{g}{2} \cdot \frac{4}{g} \cdot \sup_{z \in \Gamma} \|(\mathcal{H}(\xi) - z\mathbf{I})^{-1}\|_\infty \leq \frac{4}{1 - \epsilon_\tau} c_{\mathcal{P}} = c_{\mathcal{S}}, \end{aligned} \quad (49)$$

where we assume  $|\lambda(\xi) - 1| \leq g/4$  and  $|\lambda(\xi) - z| \geq g/4$ . Here,  $c_{\mathcal{P}}$  and  $c_{\mathcal{S}}$  serve as the upper bounds of operators echoed with (33). The assumption is justified by shrinking  $\xi$  by a constant so the Neumann condition holds on  $\Gamma_{1/4} : |z - 1| = g/4$ ; the projection bound  $\|\mathcal{P}(\xi)\|_\infty$  on  $\Gamma$  is unchanged, only the admissible step size scales. Combining with (43) (48) (49), we can bound (41) by

$$|\lambda'''(\xi)| \leq K_3. \quad (50)$$

Let  $\xi \leq \omega \leq \sqrt{\frac{3\tau}{2QK_3}}$  (the last term in (34) appears), then

$$\frac{|\lambda'''(\xi)|}{6} \omega^2 \leq \frac{\tau}{4Q}. \quad (51)$$

This leads the remainder to be absorbed, and the final rate becomes linear by  $1 - \frac{\tau}{4Q}\omega$ . The proof is complete.  $\square$

**Remark 4** (Trade-offs and choices). Because  $\lambda''(0) = 0$ , the first nontrivial stepsize restriction comes from the third-order Taylor term, controlled via  $|\lambda'''(\xi)|$ , which typically yields a sharper bound. For a more conservative guarantee, one may instead use an expansion with a second-order remainder. The choice of contour radius around  $\Gamma$  trades off the constants:  $\frac{1}{2}$  is a simple, roughly balanced option, but tuning this ratio can reduce conservatism. Using other induced norms (e.g., spectral or weighted  $\ell_\infty$ ) can tighten the constant sets in (32) and (33) and thereby enlarge the admissible range of  $\mu$ . The bound can also be simplified to an  $\mathcal{O}(\cdot)$  form by further absorbing terms in these constant sets, which we leave for future refinement. In practice, gaps are often larger and couplings smaller than in the worst case, so stable simulations typically admit stepsizes exceeding the conservative threshold in (34). Moreover, for a fixed stepsize, decreasing  $\epsilon_\tau$  can further accelerate convergence.

## 6 ACKNOWLEDGEMENTS

**Special Thanks:** The authors would like to thank Prof. Peter J. G. Teunissen for his insightful discussions during the development of the distributed GNSS framework. His conceptual suggestions greatly contributed to the early

stages of this work.

**Funding:** This work was supported by the King Abdullah University of Science and Technology (KAUST) Office of Sponsored Research (OSR) under Award No. RFS-CRG12-2024-6478.

**Competing Interests:** Tareq Y. Al-Naffouri serves as a Guest Editor for the *npj Wireless Technology* Collection “Advances in Wireless Positioning and Sensing.” He had no role in the peer review, editorial decision-making, or handling of this manuscript, which was managed independently by another editor with no competing interests. The remaining authors declare no competing interests.

**Author Contribution Statements:** Xue Xian Zheng carried out the algorithmic development and implementation, performed the theoretical analysis, ran simulations, generated figures, and co-drafted the initial manuscript. Xing Liu led the modelling/problem formulation, implemented the methods and coding, coordinated the project, co-drafted the initial manuscript, and served as the corresponding author. Tareq Y. Al-Naffouri supervised the project, provided resources, and revised the manuscript.

**Data availability:** The simulated datasets and the accompanying scenario generator will be deposited in a public repository upon publication (DOI to be provided). The input data consist of IGS station coordinates and multi-GNSS broadcast navigation files, which are publicly available from the respective providers and mirror archives.

**Code availability:** A reference implementation of Graph-Aware ATC GT-Diffusion, including Algorithm 1&2 to reproduce the figures, will be deposited in a public repository upon publication (DOI to be provided) under an open source license. Configuration files and environment/requirements files will be included to facilitate reproduction.

## APPENDIX A

### PROOF OF LEMMA 1

Multiplying  $\frac{1}{R}(\mathbf{1}^\top \otimes \mathbf{I}_d)$  on both sides of (10) and using (12), it shows

$$\begin{aligned} \bar{\mathbf{z}}^{k+1} &= \frac{1}{R}(\mathbf{1}^\top \otimes \mathbf{I}_d) \mathcal{W}^k (\mathcal{Z}^k - \mu G^k), \\ \bar{\mathbf{g}}^{k+1} &= \frac{1}{R}(\mathbf{1}^\top \otimes \mathbf{I}_d) \mathcal{W}^k G^k + \bar{\nabla} f^{k+1} - \bar{\nabla} f^k. \end{aligned} \quad (52)$$

Using the mixed product property on  $\mathcal{W}^k = \mathbf{W}^{(k\% \tau)} \otimes \mathbf{I}_d$  and  $\mathbf{1}^\top \mathbf{W}^{(k\% \tau)} = \mathbf{1}^\top$  in Assumption 2, it holds

$$\frac{1}{R}(\mathbf{1}^\top \otimes \mathbf{I}_d) \mathcal{W}^k = \frac{1}{R}(\mathbf{1}^\top \otimes \mathbf{I}_d), \quad (53)$$

Then (15) holds. Similarly, given  $\mathbf{g}_r^0 = \nabla f_r(\mathbf{z}_r^0)$ , telescoping (52) gives  $\bar{\mathbf{g}}^k = \bar{\nabla} f^k$  and hence (16). According to the definition of  $\Delta^k$  in (13), the equality in (17) holds. Since each  $f_r(\mathbf{z})$  is  $L$ -smooth by Assumption 1, we can write

$$\left\| \frac{1}{R} \sum_{r=1}^R (\nabla f_r(\mathbf{z}_r^k) - \nabla f_r(\bar{\mathbf{z}}^k)) \right\| \leq \frac{L}{R} \sum_{r=1}^R \|\mathbf{z}_r^k - \bar{\mathbf{z}}^k\|. \quad (54)$$

By Cauchy–Schwarz inequality, we further bounded

$$\frac{L}{R} \sum_{r=1}^R \|\mathbf{z}_r^k - \bar{\mathbf{z}}^k\| \leq \frac{L(\sum_{r=1}^R 1)^{1/2}}{R} \left( \sum_{r=1}^R \|\mathbf{z}_r^k - \bar{\mathbf{z}}^k\|^2 \right)^{1/2} \quad (55)$$

of which the r.h.s is  $\frac{L}{\sqrt{R}} \|\mathcal{C}^k\|$ . The proof is completed.  $\square$

## APPENDIX B

### PROOF OF LEMMA 2

Merging (15)-(16), we can write

$$\bar{\mathbf{z}}^{k+1} = \bar{\mathbf{z}}^k - \mu \nabla F(\bar{\mathbf{z}}^k) - \mu \Delta^k. \quad (56)$$

Subtracting  $\mathbf{z}^*$  from (56) and inserting  $\nabla F(\mathbf{z}^*) = 0$  into the r.h.s., it holds

$$\mathbf{s}^{k+1} = (\mathbf{I}_d - \mu \mathbf{H}) \mathbf{s}^k - \mu \Delta^k, \quad (57)$$

Under Assumption 1,  $F(\mathbf{z})$  is  $m$ -strongly convex and  $L$ -smooth ( $m\mathbf{I}_d \preceq \nabla^2 F(\mathbf{z}) \preceq L\mathbf{I}_d$ ), and hence for  $\mu \leq 1/L$ ,

$$(1 - \mu L)\mathbf{I}_d \preceq \mathbf{I}_d - \mu \mathbf{H} \preceq (1 - \mu m)\mathbf{I}_d. \quad (58)$$

Using (57) and the triangle inequality,

$$\begin{aligned} \|\mathbf{s}^{k+1}\| &= \|(\mathbf{I}_d - \mu \mathbf{H}) \mathbf{s}^k - \mu \Delta^k\| \\ &\leq \|(\mathbf{I}_d - \mu \mathbf{H}) \mathbf{s}^k\| + \mu \|\Delta^k\| \stackrel{(58)}{\leq} (1 - \mu m) \|\mathbf{s}^k\| + \mu \|\Delta^k\|. \end{aligned} \quad (59)$$

Finally, by (17),  $\|\Delta^k\| \leq \frac{L}{\sqrt{R}} \|\mathcal{C}^k\|$ , which yields the stated second inequality.  $\square$

## APPENDIX C

### PROOF OF LEMMA 3

Multiplying  $\mathcal{J}_\perp$  on both sides of the first line in (10), using  $\mathcal{J}_\perp \mathcal{W}^k = (\mathcal{W}^k - \mathcal{J})$  and  $\mathcal{J}_\perp \mathcal{J} = \mathbf{0}$ , we obtain

$$\begin{aligned} \mathcal{C}^{k+1} &= \mathcal{J}_\perp \mathcal{Z}^{k+1} = (\mathcal{W}^k - \mathcal{J})(\mathcal{Z}^k - \mu G^k) \\ &= (\mathcal{W}^k - \mathcal{J})(\mathcal{C}^k - \mu \mathcal{T}^k). \end{aligned} \quad (60)$$

Iterating over  $\{(i-1)\tau, \dots, k-1, k\}$ , it follows that

$$\begin{aligned} \mathcal{C}^k &= \left( \prod_{j=i\tau}^{k-1} (\mathcal{W}^j - \mathcal{J}) \right) \left( \prod_{j=(i-1)\tau}^{i\tau-1} (\mathcal{W}^j - \mathcal{J}) \right) \mathcal{C}^{(i-1)\tau} \\ &\quad - \mu \sum_{j=(i-1)\tau}^{k-1} \left( \prod_{t=j}^{k-1} (\mathcal{W}^t - \mathcal{J}) \right) \mathcal{T}^j. \end{aligned} \quad (61)$$

where  $\prod$  is the left-wise product. Taking the spectral norm on (61), using submultiplicativity together with

$$\begin{aligned} \|\mathcal{W}^j - \mathcal{J}\| &= \|(\mathbf{W}^{(j\% \tau)} - \frac{1}{R} \mathbf{1}\mathbf{1}^\top) \otimes \mathbf{I}_d\| \leq 1 \\ \left\| \prod_{j=(i-1)\tau}^{i\tau-1} (\mathcal{W}^j - \mathcal{J}) \right\| &= \left\| \left( \prod_{j=0}^{\tau-1} \mathbf{W}^j - \frac{1}{R} \mathbf{1}\mathbf{1}^\top \right) \otimes \mathbf{I}_d \right\| = \epsilon_\tau \end{aligned} \quad (62)$$

from Assumption 2 yields (19).  $\square$

## APPENDIX D

### PROOF OF LEMMA 4

Similar to (60), we can write

$$\mathcal{T}^{k+1} = (\mathcal{W}^k - \mathcal{J})\mathcal{T}^k + \mathcal{J}_\perp(\nabla\mathcal{F}^{k+1} - \nabla\mathcal{F}^k). \quad (63)$$

Iterating over  $\{(i-1)\tau, \dots, k-1, k\}$ , and using  $\mathcal{J}_\perp \mathcal{W}^k = \mathcal{W}^k \mathcal{J}_\perp$  and  $\mathcal{J}_\perp \mathcal{J} = \mathbf{0}$ , it follows that

$$\begin{aligned} \mathcal{T}^k &= \left( \prod_{j=i\tau}^{k-1} (\mathcal{W}^j - \mathcal{J}) \right) \left( \prod_{j=(i-1)\tau}^{i\tau-1} (\mathcal{W}^j - \mathcal{J}) \right) \mathcal{T}^{(i-1)\tau} \\ &+ \sum_{j=(i-1)\tau}^{k-1} \left( \prod_{t=j+1}^{k-1} (\mathcal{W}^t - \mathcal{J}) \right) (\nabla\mathcal{F}^{j+1} - \nabla\mathcal{F}^j). \end{aligned} \quad (64)$$

Taking the spectral norm and using (62), we write

$$\|\mathcal{T}^k\| \leq \epsilon_\tau \|\mathcal{T}^{(i-1)\tau}\| + \sum_{j=(i-1)\tau}^{k-1} \|\nabla\mathcal{F}^{j+1} - \nabla\mathcal{F}^j\|. \quad (65)$$

By  $L$ -smoothness,

$$\|\nabla\mathcal{F}^{j+1} - \nabla\mathcal{F}^j\| \leq L \|\mathcal{Z}^{j+1} - \mathcal{Z}^j\|. \quad (66)$$

By (10),  $\mathcal{Z}^{j+1} - \mathcal{Z}^j = (\mathcal{W}^j - \mathbf{I}_{Rd}) \mathcal{Z}^j - \mu \mathcal{W}^j G^j$ , and we can decompose  $\mathcal{Z}^j = \mathcal{C}^j + \mathbf{1} \otimes \bar{\mathbf{z}}^j$  with  $(\mathcal{W}^j - \mathbf{I}_{Rd})(\mathbf{1} \otimes \bar{\mathbf{z}}^j) = \mathbf{0}$ , it therefore holds

$$\begin{aligned} \|\mathcal{Z}^{j+1} - \mathcal{Z}^j\| &\leq \underbrace{\|\mathcal{W}^j - \mathbf{I}_{Rd}\|_{\mathcal{J}_\perp}}_{\leq c_W \leq 2} \|\mathcal{C}^j\| + \underbrace{\mu \|\mathcal{W}^j\|}_{\leq 1} \|G^j\|. \end{aligned} \quad (67)$$

Decomposing  $G^j = \mathcal{T}^j + \mathcal{J}G^j$  and using  $\|\mathcal{J}G^j\| = \sqrt{R} \|\bar{\mathbf{g}}^j\|$  with  $\bar{\mathbf{g}}^j = \nabla f^j = \nabla F(\bar{\mathbf{z}}^j) + \Delta^j$  from Lemma 1, we bound

$$\begin{aligned} \|G^j\| &\leq \|\mathcal{T}^j\| + \sqrt{R} \|\bar{\mathbf{g}}^j\| \\ &\leq \|\mathcal{T}^j\| + \sqrt{R} (L \|\mathbf{s}^j\| + \frac{L}{\sqrt{R}} \|\mathcal{C}^j\|), \end{aligned} \quad (68)$$

where we used  $L$ -smoothness of  $F(\mathbf{z})$  and (17). Combining (66)–(68),

$$\begin{aligned} \|\nabla\mathcal{F}^{j+1} - \nabla\mathcal{F}^j\| &\leq L c_W \|\mathcal{C}^j\| + \mu L^2 \|\mathcal{C}^j\| \\ &+ \mu L \|\mathcal{T}^j\| + \mu \sqrt{R} L^2 \|\mathbf{s}^j\|. \end{aligned} \quad (69)$$

Plugging (69) into (65) yields, for any  $k \in \{i\tau, \dots, (i+1)\tau\}$ ,

$$\begin{aligned} \|\mathcal{T}^k\| &\leq \epsilon_\tau \|\mathcal{T}^{(i-1)\tau}\| + \sum_{j=(i-1)\tau}^{k-1} \left( L c_W \|\mathcal{C}^j\| + \mu L^2 \|\mathcal{C}^j\| \right. \\ &\left. + \mu L \|\mathcal{T}^j\| + \mu \sqrt{R} L^2 \|\mathbf{s}^j\| \right). \end{aligned} \quad (70)$$

Switching terms, (20) then follows.  $\square$

## REFERENCES

- [1] P. Héroux and J. Kouba, *GPS precise point positioning with a difference*. Natural Resources Canada, Geomatics Canada, Geodetic Survey Division Ottawa . . . , 1995.
- [2] J. F. Zumberge, M. B. Heflin, D. C. Jefferson, M. M. Watkins, and F. H. Webb, "Precise point positioning for the efficient and robust analysis of GPS data from large networks," *Journal of geophysical research: solid earth*, vol. 102, no. B3, pp. 5005–5017, 1997.
- [3] G. Wabben, M. Schmitz, and A. Bagge, "PPP-RTK: precise point positioning using state-space representation in RTK networks," in *Proceedings of the 18th international technical meeting of the satellite division of the Institute of navigation (ION GNSS 2005)*, 2005, pp. 2584–2594.
- [4] P. J. Teunissen, D. Odijk, and B. Zhang, "PPP-RTK: results of CORS network-based PPP with integer ambiguity resolution," *J Aeronaut Astronaut Aviat Ser A*, vol. 42, no. 4, pp. 223–230, 2010.
- [5] D. Laurichesse, F. Mercier, J.-P. Berthias, P. Broca, and L. Cerri, "Integer ambiguity resolution on undifferenced GPS phase measurements and its application to PPP and satellite precise orbit determination," *Navigation*, vol. 56, no. 2, pp. 135–149, 2009.
- [6] P. Collins, S. Bisnath, F. Lahaye, and P. Héroux, "Undifferenced GPS ambiguity resolution using the decoupled clock model and ambiguity datum fixing," *Navigation*, vol. 57, no. 2, pp. 123–135, 2010.
- [7] L. Ries, M. C. Limon, F.-C. Grec, M. Anghileri, R. Prieto-Cerdeira, F. Abel, J. Miguez, J. V. Perello-Gisbert, S. D'Addio, R. Ioannidis, A. Ostillio, M. Rapisarda, R. Sarnadas, and P. Testani, "LEO-PNT for augmenting europe's space-based PNT capabilities," in *2023 IEEE/ION Position, Location and Navigation Symposium (PLANS)*, 2023, pp. 329–337.
- [8] W. Stock, R. T. Schwarz, C. A. Hofmann, and A. Knopp, "Survey on opportunistic PNT with signals from LEO communication satellites," *IEEE Communications Surveys & Tutorials*, vol. 27, no. 1, pp. 77–107, 2025.
- [9] Z. M. Kassas, S. Kozhaya, H. Kanj, J. Saroufim, S. W. Hayek, M. Neinavaie, N. Khairallah, and J. Khalife, "Navigation with multi-constellation leo satellite signals of opportunity: Starlink, oneweb, orbcomm, and iridium," in *2023 IEEE/ION Position, Location and Navigation Symposium (PLANS)*, 2023, pp. 338–343.
- [10] A. H. Sayed, "Diffusion adaptation over networks," in *Academic Press Library in Signal Processing*. Elsevier, 2014, vol. 3, pp. 323–453.
- [11] R. Olfati-Saber, J. A. Fax, and R. M. Murray, "Consensus and cooperation in networked multi-agent systems," *Proceedings of the IEEE*, vol. 95, no. 1, pp. 215–233, 2007.
- [12] G. Wood *et al.*, "Ethereum: A secure decentralised generalised transaction ledger," *Ethereum project yellow paper*, vol. 151, no. 2014, pp. 1–32, 2014.
- [13] B. McMahan, E. Moore, D. Ramage, S. Hampson, and B. A. y Arcas, "Communication-efficient learning of deep networks from decentralized data," in *Artificial intelligence and statistics*. PMLR, 2017, pp. 1273–1282.
- [14] M. Rubenstein, A. Cornejo, and R. Nagpal, "Programmable self-assembly in a thousand-robot swarm," *Science*, vol. 345, no. 6198, pp. 795–799, 2014.
- [15] H. Boomkamp, "Distributed processing for large geodetic solutions," in *Reference Frames for Applications in Geosciences*. Springer, 2012, pp. 13–18.
- [16] A. Khodabandeh, P. J. Teunissen, and S. Zaminpardaz, "Consensus-based distributed filtering for gnss," in *Kalman filters-theory for advanced applications*. IntechOpen, 2017.
- [17] A. Khodabandeh and P. Teunissen, "Distributed least-squares estimation applied to GNSS networks," *Measurement Science and Technology*, vol. 30, no. 4, p. 044005, 2019.

- [18] P. Hou and B. Zhang, "Decentralized GNSS PPP-RTK," *Journal of Geodesy*, vol. 97, no. 7, p. 72, 2023.
- [19] R. Nassif, S. Vlaski, C. Richard, J. Chen, and A. H. Sayed, "Multi-task learning over graphs: An approach for distributed, streaming machine learning," *IEEE Signal Process. Mag.*, vol. 37, no. 3, pp. 14–25, 2020.
- [20] S. Vlaski, S. Kar, A. H. Sayed, and J. M. Moura, "Networked signal and information processing: Learning by multiagent systems," *IEEE Signal Process. Mag.*, vol. 40, no. 5, pp. 92–105, 2023.
- [21] J. M. Hendrickx, R. M. Jungers, A. Olshevsky, and G. Vankeerberghen, "Graph diameter, eigenvalues, and minimum-time consensus," *Automatica*, vol. 50, no. 2, pp. 635–640, 2014.
- [22] A. Fainman and S. Vlaski, "Learned finite-time consensus for distributed optimization," in *2024 32nd European Signal Processing Conference (EUSIPCO)*. IEEE, 2024, pp. 1047–1051.
- [23] B. Ying, K. Yuan, Y. Chen, H. Hu, P. Pan, and W. Yin, "Exponential graph is provably efficient for decentralized deep training," *Advances in Neural Information Processing Systems*, vol. 34, pp. 13 975–13 987, 2021.
- [24] E. D. H. Nguyen, X. Jiang, B. Ying, and C. A. Uribe, "On graphs with finite-time consensus and their use in gradient tracking," *SIAM Journal on Optimization*, vol. 35, no. 2, pp. 872–898, 2025.
- [25] L. Liang, X. Huang, R. Xin, and K. Yuan, "Understanding the influence of digraphs on decentralized optimization: Effective metrics, lower bound, and optimal algorithm," *SIAM Journal on Optimization*, vol. 35, no. 3, pp. 1570–1600, 2025.
- [26] D. Odijk, B. Zhang, A. Khodabandeh, R. Odolinski, and P. J. Teunissen, "On the estimability of parameters in undifferenced, uncombined GNSS network and PPP-RTK user models by means of S-system theory," *Journal of Geodesy*, vol. 90, no. 1, pp. 15–44, 2016.
- [27] A. Nedic, A. Olshevsky, and W. Shi, "Achieving geometric convergence for distributed optimization over time-varying graphs," *SIAM Journal on Optimization*, vol. 27, no. 4, pp. 2597–2633, 2017.
- [28] S. Boyd, P. Diaconis, P. Parrilo, and L. Xiao, "Fastest mixing markov chain on graphs with symmetries," *SIAM Journal on Optimization*, vol. 20, no. 2, pp. 792–819, 2009.
- [29] P. A. Knight, "The sinkhorn–knopp algorithm: convergence and applications," *SIAM Journal on Matrix Analysis and Applications*, vol. 30, no. 1, pp. 261–275, 2008.
- [30] M. Cuturi, "Sinkhorn distances: Lightspeed computation of optimal transport," *Advances in neural information processing systems*, vol. 26, 2013.
- [31] A. Koloskova, T. Lin, and S. U. Stich, "An improved analysis of gradient tracking for decentralized machine learning," *Advances in Neural Information Processing Systems*, vol. 34, pp. 11 422–11 435, 2021.
- [32] K. He, X. Zhang, S. Ren, and J. Sun, "Deep residual learning for image recognition," in *Proceedings of the IEEE conference on computer vision and pattern recognition*, 2016, pp. 770–778.
- [33] G. A. Watson, "Characterization of the subdifferential of some matrix norms," *Linear Algebra Appl*, vol. 170, no. 1, pp. 33–45, 1992.
- [34] T. Kato, *Perturbation theory for linear operators*. Springer Science & Business Media, 2013, vol. 132.
- [35] G. W. Stewart, *Perturbation theory for the singular value decomposition*. University of Maryland at College ParkCollege Park, MDUnited States, 1990.
- [36] A. Greenbaum, R.-c. Li, and M. L. Overton, "First-order perturbation theory for eigenvalues and eigenvectors," *SIAM review*, vol. 62, no. 2, pp. 463–482, 2020.
- [37] F. Riesz and B. S. Nagy, *Functional analysis*. Courier Corporation, 2012.